Check for updates

Geochemical implications for gas hydrate occurrence and seepage at Sites GMGS5-W07 and W09 in Qiongdongnan Basin, South China Sea

Yinghan Lu[1,2], Hailin Yang[1,2]*, Hailong Lu[1,2]*, Yunxin Fang[3,4]* and Zenggui Kuang[3,4]

[1]School of Earth and Space Sciences, Peking University, Beijing, China, [2]Beijing International Center for Gas Hydrate, Beijing, China, [3]Guangzhou Marine Geology Survey, Guangzhou, China, [4]Southern Marine Science and Engineering Guangdong Laboratory, Guangzhou, China

The compositions and morphological characteristics of minerals and the cycle of trace elements in sedimentary environments are considered to be powerful indicators for the occurrence and evolution of gas hydrates. In this article, total organic carbon (TOC) content, particle size distribution, mineral composition, element distribution, and iron speciation of sediments from sites GMGS5-W07 and GMGS5-W09 of the South China Sea are studied. The high content of TOC and the occurrence of authigenic mineral assemblages suggest the accumulation potential of gas hydrate at the two sites. In the methane-rich layers, redox-sensitive trace elements, such as Co, Ni, Cu, Zn, As, Sb, Fe, and Mn, are enriched while reducing conditions lead to the accumulation of Fe and the increase of Fe(II) species proportion in sediments. Enrichment factors and Pearson correlation analysis of trace elements show that the circulation of trace elements at site W07 is more strongly affected by methane-rich fluids than at site W09. Fe-oxyhydroxides play a critical role in the development of As and Sb enrichments, and in particular, seep fluids may be a pivotal extra input of Mo, As, and Sb at site W07. Therefore, more intense methane seepage might have happened at site W07, and this conjecture has been further confirmed by higher Sr/Ca in sediments. Based on these results, the change in seepage intensity is not associated with the occurrence of gas hydrate.

KEYWORDS

gas hydrate, seepage, South China Sea, Fe species, trace elements, authigenic minerals, particle size

1 Introduction

The geochemical conditions of gas hydrate-bearing sediments have been recognized, which have also been known to affect the formation of authigenic mineral and the behaviors of elements. In recent years, a scientific geochemical method of identifying gas hydrate-bearing environments has been established through a series of proxies, including but not limited to organic carbon content, authigenic minerals, and element composition (Chen et al., 2016; Feng and Chen, 2015; Himmler et al., 2013; Li N et al., 2016; Liu et al., 2020; Smrzka et al., 2020; Tong et al., 2013; Wang et al., 2018).

Sediment granularity is an important factor influencing gas hydrate saturation, and the suitable reservoir is in favor of gas hydrate storage (Ginsburg et al., 2000; Lu et al., 2011). It is generally stored in coarse-grained sediments, such as sand deposits with high porosity and methane seepage (Collett et al., 1988; Uchida and Tsuji, 2004; Boswell, 2007). However, numerous submarine gas hydrate may be stored in the clay (<4 μm) and silt (4–63 μm) of fine-grained sediments, and gas hydrate has the characteristics of small thickness and low saturation with disseminated structure (Shaohua et al., 2015). Some studies showed that there may be a good corresponding relationship between the microbiological shell and a relatively large layer of fine-grained sediments with gas hydrate, such as Blake Ridge in the western Atlantic Ocean (Kraemer et al., 2000) and the South China Sea (Zhang et al., 2007; Li C et al., 2016).

A special mineral assemblage has been confirmed in the gas hydrate- or seepage-impact environment. In general, minerals commonly found in gas hydrate-bearing environments include authigenic carbonate minerals (e.g., calcite, dolomite, aragonite, and high-Mg calcite), sulfate minerals (e.g., gypsum and barite), and pyrite (Ritger et al., 1987; Peckmann et al., 2001; Luff and Wallmann, 2003; Egawa et al., 2015; Feng and Chen, 2015; Zhou et al., 2020). These minerals are thought to be the products of sulfate-dependent anaerobic oxidation of methane (AOM, Eq. 1, Boetius et al., 2000; Devol and Ahmed, 1981; Murray et al., 1978), and this process increases the alkalinity of the environment and provides anions for the formation of authigenic minerals. AOM is the most typical reaction that occurs at the sulfate-methane transition zone (SMTZ) (Knittel and Boetius, 2009) or might proceed in the gas hydrate zone (Cui et al., 2019) and is also strongly affected by the seepage strength (Joye et al., 2004; Boetius and Wenzhöfer, 2013). For the abovementioned reasons, authigenic minerals are critical geochemical proxies closely related to the hydrate deposition environments and can indicate the presence of gas hydrate and methane upwelling to a certain extent (Feng and Chen, 2015; Zhang et al., 2018; Zhou et al., 2020).

$$CH_4 + SO_4^{2-} \rightarrow HCO_3^- + HS^- + H_2O \qquad (1)$$
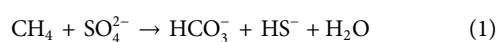
Deposition area where gas hydrates exist and methane seepage have occurred will affect the circulation of elements in sediments, especially redox-sensitive trace elements (Tribovillard et al., 2006; Tribovillard et al., 2013; Hu et al., 2015b; Chen et al., 2016; Smrzka et al., 2020). Past research has shown that redox-sensitive elements such as Mo, U, and V are strongly enriched under anoxic conditions, and to a lesser extent, certain other trace metals like Cr and Co are also classified to judge the oxidation and reduction environments (Tribovillard et al., 2006; Algeo and Tribovillard, 2009; Tribovillard et al., 2012). Ni, Cu, Zn, and Cd are mainly associated with organic matter, and may be reserved to the sediment in association with pyrite after the reduction processes decompose organic matter (Tribovillard et al., 2006). Under normal circumstances, Ba and P in the ocean environment can evaluate the level of paleoproductivity, while sedimentary environments with gas hydrate are often accompanied by high organic matter fluxes (Dymond et al., 1992; Tribovillard et al., 2006).

Otherwise, the geochemical cycling of Fe is redox-active in near-surface marine sediments and methane-rich layers (Froelich et al., 1979; Raiswell and Canfield, 2012; Riedinger et al., 2014; Hu et al., 2015a; Nevin and Lovley, 2002). Under normal reducing conditions, Fe exists mainly in divalent cationic form and forms sulfide or sometimes siderite. Under oxidizing conditions, Fe^{2+} will be oxidized to Fe^{3+} and mainly deposited as hydroxides or oxides, such as hematite and goethite, respectively (Nevin and Lovley, 2002; Hedrich et al., 2011). In sediments affected by sulfidic conditions, the precipitation of Fe sulfides is favorable, which leads to authigenic Fe accumulation (Scholz et al., 2014a, b), namely, Fe-oxyhydroxides and ferrous Fe, which will experience the circulation of reprecipitation and redissolution and release into the pore water among oxic zone, suboxic zone, and sulfidic zone. Methane seepages could represent a source of dissolved Fe to the deep ocean with the amount of Fe released into seawater from methane fluids (Lemaitre et al., 2014). In such environments, the release of hydrogen sulfide and bicarbonate through AOM leads to the reduction of Fe-oxyhydroxides and the precipitation of Fe sulfides (Hensen et al., 2003; März et al., 2008; Yang et al., 2018). Based on this, Fe speciation could be regarded as a tool to assess variable redox conditions during seepage history (Hu et al., 2015a). In addition, Fe speciation also contributes to the interpretation of fluctuations of redox-sensitive elements in the seepage-impact environment under various redox conditions. The mobilization of Fe (oxyhydr)oxide-bound P has been reported around the SMTZ (März et al., 2008), and the enrichment of some redox-sensitive elements, such as, Sb, and Mo, has a link with the adsorption of Fe-oxyhydroxides (Dymond et al., 1992; Tribovillard et al., 2013; Hu et al., 2014).

Geochemical methods such as elemental content, mineral composition, and TOC content in seafloor sediments have long been a critical scientific tool for revealing gas hydrate accumulation and methane seepage in the study area. In this article, we compared the sediment's total organic carbon contents, particle size compositions, authigenic minerals, and

trace elements contents of two adjacent sites with different hydrate accumulation circumstances (gas hydrate content and seepage activity) on the north slope of the South China Sea during the fifth "China Gas Hydrate Drilling Expedition" (GMGS5) in 2018. Different from previous research, our work provides an opportunity to distinguish the geochemical conditions under different scenarios of gas hydrate occurrence and seepage evolution.

2 Geological setting and gas hydrate occurrence in the Qiongdongnan Basin

2.1 Geological setting

Benefitting from the widely distributed sedimentary basins, various faults or diapir structures and adequate organic matter supply, the northern continental slope of the South China Sea (SCS) is not only rich in oil and gas but also a hotspot for the exploration and exploitation of gas hydrates (Zhang et al., 2002; Wu et al., 2005; Wang et al., 2006). From now on, China has considerable reserves of gas hydrate in the SCS, including Xisha Sea Area (XSA), Shenhu Sea Area (SSA), Dongsha Sea Area (DSA), Pearl River Mouth Basin (PRMB), and Qiongdongnan Basin (QDNB) (Zhang et al., 2002; Jiang et al., 2008; Wu et al., 2008; Li et al., 2013; Liu et al., 2014; Zhang et al., 2015; Xu et al., 2016; Fang et al., 2019; Wei et al., 2019).

The Qiongdongnan Basin (QDNB), which is located at the northeast continental shelf of the SCS, covers an area of approximately 65,000 km^2. The water depth varies considerably, and the sedimentation rate is high (Ye et al., 1985; Zhao et al., 1999). The pre-Cenozoic basement of the QDNB is composed of Paleozoic metamorphic rocks, dolomites, cretaceous intermediate-acid granites, diorites, and volcanic clastic rocks (Huang et al., 2016). The sedimentary sequences include Paleogene, Neogene, and Quaternary strata (Zhu et al., 2009). Through petroleum explorations, benefitting from the extensive surface sea deposits and continental shelf slope deposits, the QDNB has good gas hydrate generation and storage capacity, especially the Eocene and Oligocene Yacheng formations are the main source rocks (Zhu et al., 2009; Su et al., 2012; Huang et al., 2016).

2.2 Gas hydrate expedition in the Qiongdongnan Basin

Since 2007, the Guangzhou Marine Geological Survey (GMGS) has carried out five gas-hydrate drilling expeditions in the SCS, the survey area includes eastern PRMB, XSA, SSA, and QDNB (Sha et al., 2015; Zhang et al., 2015; Wei et al., 2018; Wei et al., 2019). Through comprehensive survey methods of geology, geophysics, geochemistry, and biological characteristics, multilevel and multi-information abnormal signs related to gas hydrate were discovered. Research of the bottom simulating reflection (BSR) (Liang et al., 2019), the abnormal chemical composition of pore water (Sun et al., 2007), active cold seeps (Liang et al., 2017; Fang et al., 2019), authigenic carbonate minerals (Chen et al., 2016; Liang et al., 2017), and mud diapirs and gas chimneys (Zhang et al., 2019) have confirmed that the QDNB is rich in gas hydrate resources. In addition, sediments in which gas hydrates-recovered in the QDNB were dominated by clay and fine silt (Liang et al., 2019; Wei et al., 2019; Ye et al., 2019), and mainly exist in various fractures (Wei et al., 2021).

In 2018, the fifth gas hydrate drilling expedition (GMGS5) in the northwestern continental slope of the SCS was conducted by GMGS (Figure 1A). Four sites (W01, W07, W08, and W09) were selected to drill six boreholes (W01B, W07B, W08B, W08C, W09B, and W09C) in this investigation. In particular, vast quantities of gas hydrates were discovered and collected at site W08, which was the most typical and representative gas hydrate site drilled during this investigation (Wei et al., 2019; Lai et al., 2021). The samples in this article come from site W07 and W09 (Table 1), all of which are at the depth of 1,600–1,800 m in the deep water of the eastern part of the QDNB (Figure 1B). The seabed terrain is relatively flat (1.3–2.8 of W-E slope), which is conducive to the accumulation of gas hydrates (Wei et al., 2019). The seismic profile shows that, influenced by the position of the Songnan Low Uplift, site W07 and W09 were both drilled through the seepage pathways on the two chimneys (Liang et al., 2019; Wei et al., 2021).

Near site W09, active clams and a mound-like structure were observed, while life activity was limited (Wei et al., 2021). Confirmed by the coring and sampling results and pilot hole logging while drilling (LWD) anomalies, gas hydrates existed at the depth of 7–158 mbsf (Liang et al., 2019). The gas hydrate content increased with depth and showed a bump in the middle layer (from 60 mbsf to 100 mbsf, Figure 1C), multiple layers exhibited very high gas hydrate content (up to >80%) (Wei et al., 2019), which were dominated by fracture-filling hydrate (Wei et al., 2021).

There were many pockmarks near site W07, but no obvious traces of life activity were found (Wei et al., 2021). The core data from site W07 showed that gas hydrate was present at 6–8% of pore volume at depths with elevated LWD resistivities (Wei et al., 2021). Low saturation hydrates were present at site W07 and gas hydrate saturation increased with depth from the seafloor to the end of the hole (Wei et al., 2019; Wei et al., 2021) (Figure 1C).
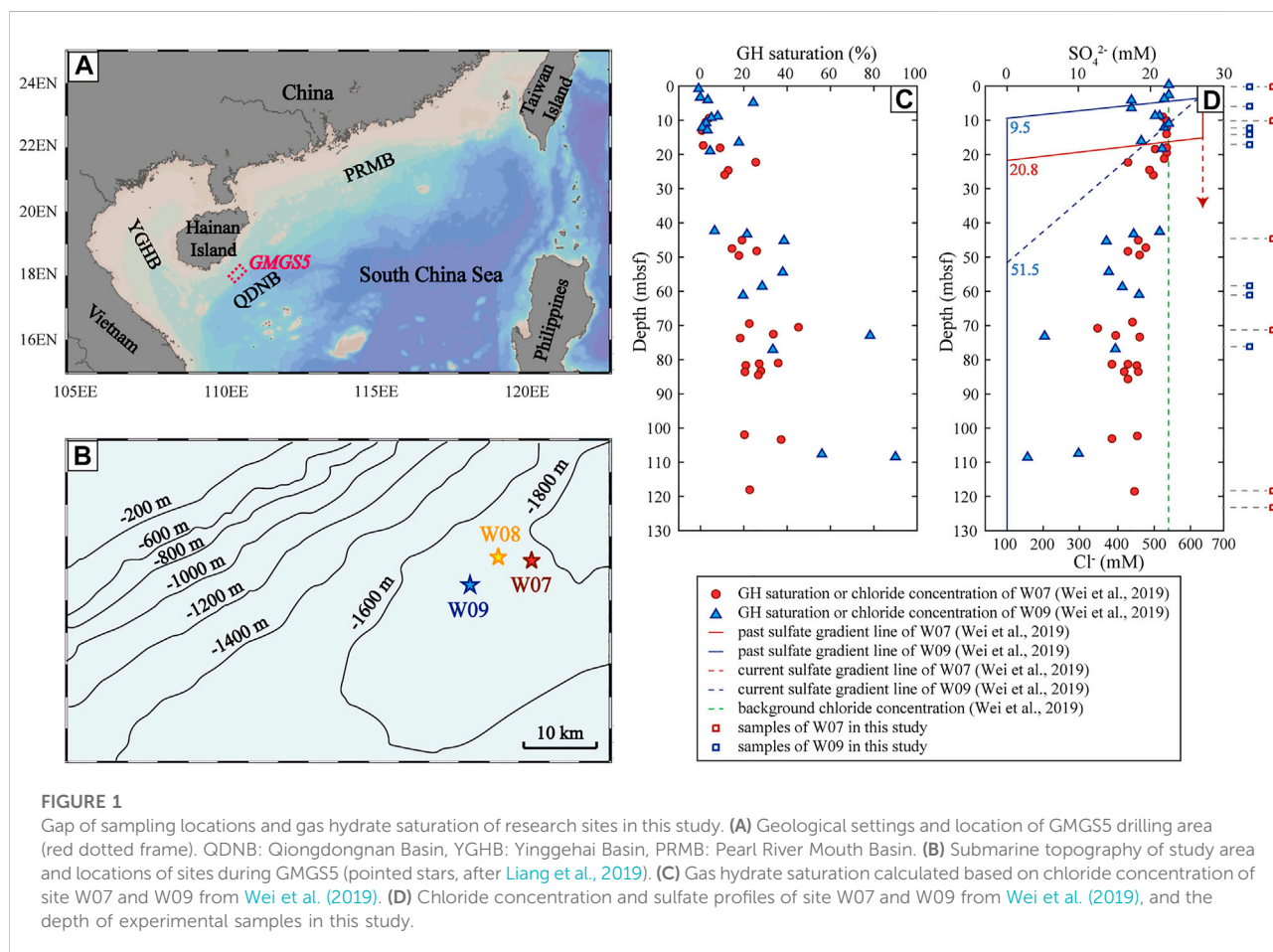
Estimated gas hydrate contents at site W09 were higher than W07, whether it was based on the chloride concentration or degassing (Wei et al., 2019). Both site W07 and W09 have kick-type sulfate profiles, positive chloride anomalies in the shallow sediment (Figure 1D), and authigenic carbonates at multiple layers, which may indicate that dynamic changes in fluid flux and

TABLE 1 Information of samples from site GMGS5-W07 and GMGS5-W09.

Site	Samples	Depth/mbsf	Water depth/mbsf	[a]SMI depth/mbsf	[a]TGHOZ depth/mbsf	[a]AGHS/m³	[b]BSR depth/mbsf
W07	W07B-1	0.00	~1775	20.05	22.5	13.70 and 3.03	142
	W07B-2	9.75					
	W07B-3	44.23					
	W07B-4	70.95					
	W07B-5	118.00					
	W07B-6	122.85					
W09	W09B-1	0.00	~1722	9.19	12.5	22.24 and 16.25	148
	W09B-2	5.50					
	W09B-3	11.90					
	W09B-4	13.75					
	W09B-5	16.70					
	W09B-6	58.00					
	W09B-7	60.75					
	W09B-8	75.75					

[a]As reported by Wei et al., (2019). TGHOZ, the top of the gas hydrate occurrence zone; AGHS, the average gas hydrate saturation, estimated using chloride concentration and degassing, respectively.
[b]As reported by Wei et al. (2021).

FIGURE 1
Gap of sampling locations and gas hydrate saturation of research sites in this study. **(A)** Geological settings and location of GMGS5 drilling area (red dotted frame). QDNB: Qiongdongnan Basin, YGHB: Yinggehai Basin, PRMB: Pearl River Mouth Basin. **(B)** Submarine topography of study area and locations of sites during GMGS5 (pointed stars, after Liang et al., 2019). **(C)** Gas hydrate saturation calculated based on chloride concentration of site W07 and W09 from Wei et al. (2019). **(D)** Chloride concentration and sulfate profiles of site W07 and W09 from Wei et al. (2019), and the depth of experimental samples in this study.

multistage gas hydrate evolution occurred on a time scale from months to thousands of years (Borowski et al., 1996; Torres et al., 1996; Fischer et al., 2013; Wei et al., 2019). Due to the increased fluid flux, gas hydrates were expected to be formed in the shallow sediment at site W07 and W09 (Wei et al., 2019). Methane seepage at the two sites accumulated the release of H_2S, causing the SMTZ to be shallow and the sedimentary environment to be reducible (Wei et al., 2019). Moreover, the seepage in site W07 was younger than W09, indicating that there may exist more free gas in W07 (Wei et al., 2021).

3 Methodology

3.1 Particle size analysis

The particle size distribution was determined *via* dynamic image analysis (CAMSIZER X2, Retsch Technology GmbH, 42,781 Haan, Retsch-Allee 1-5, Germany) at the School of Ocean Sciences, China University of Geosciences (Beijing) (CUGB). The sample preparation process sequence is as follows: 0.2000 ± 0.0010 g of the sample was accurately weighed into a 50 ml beaker, and a small amount of ultrapure water was added to immerse the sample. 10 ml of 30% H_2O_2 was added to each beaker and soaked for about 24 h to remove organic carbon. To remove the remaining H_2O_2, the sample was heated and boiled for 5min; 2 ml of 30% HCl was added to remove $CaCO_3$ after cooling. After standing for 24 h, 2 g of NaOH was added to remove biogenic opal. The sediment composition and mean particle size were obtained, and the classification and naming of the sediments adopt the Folk classification method (Folk et al., 1970).

3.2 Total organic carbon analysis

The total organic carbon (TOC) content of each sediment sample was determined using Elementar Vario TOC (Germany) at the School of Ocean Sciences, CUGB, following the procedure described by: 0.0200 ± 0.0005 g powdered sample was weighed into the tin foil cup, excess of 10% HCl was added to the tin foil cup to remove $CaCO_3$, was allowed to stand for 24 h; the cup was washed with distilled water and placed it in an oven for drying; and the tin foil cup was folded into a small square and text by the total organic carbon analyzer. Parallel samples, blank samples, and standard samples (GBW07312) were also analyzed for quality control, with the relative errors of all samples being within 2%.

3.3 Mineral analysis

X-ray diffraction (XRD) analysis of the samples was carried out using an X-ray diffractometer (Bruker D2 phaser, Germany)

at the School of Ocean Sciences, CUGB. The scanning parameters: Cu-Kα radiation (λ = 0.154 nm), 2θ scan range 5°–70°, accelerating voltage 30 kV, current 10 mA, scan speed 2°/min, sampling step 0.02°.

The morphological properties of sediment samples were observed by field emission scanning electron microscope (FESEM) analysis using a Hitachi SU8220 FESEM at State Key Laboratory of Tribology, Tsinghua University. The images were taken using a 10 kV accelerating voltage with ~180 K × magnification.

3.4 Major and trace element analysis

Major and trace elements in sediments were determined by inductively coupled plasma optical emission spectroscopy (ICP-OES, IRIS Intrepid II, Thermo Scientific) at the School of Earth and Space Sciences, Peking University. Accuracy of the major and trace elements results within 5%–10%. Among them, the different chemical species of Fe in sediments were extracted in the sequential extraction method as described by Poulton and Canfield (2005) and Yang et al. (2018), each step is shown in Table 2. To ensure the reliability of the experimental results, the results were acceptable when the yield was between 80 and 120% (Poulton and Canfield, 2005; Larner et al., 2006; Claff et al., 2010).
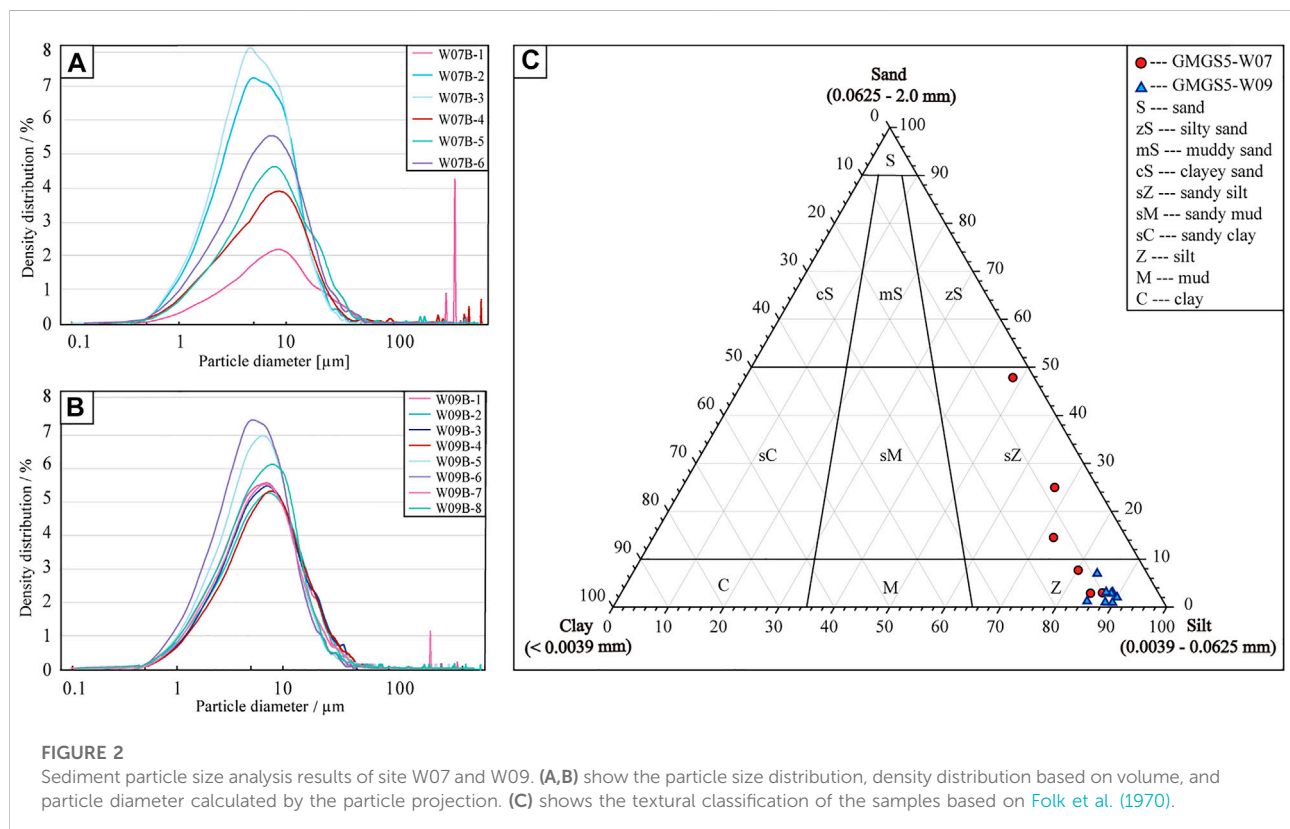
4 Results

4.1 Particle size distribution

The average size of site W07 particles was measured to be 16.75–181.63 μm, with a wide range of particle size distribution. The silt was the dominant particle size overall, with an average between 48.67% and 86.93%, while sand was the second component, with a content of 2.75%–47.63%. The particle size distribution of site W09 was in the range of 14.27–28.85 μm, with a narrow range distribution. The first component was dominated by silt, with content of 83.90–90.00%, while the second component was dominated by clay, with content of 7.95–13.73%.

Overall, the sediment particles at site W07 were coarser than at W09, and the range of particle size distribution with depth changed more widely (Figures 2A,B). The surface sediments at site W07 were the most special among all layers, with the highest sand content (47.63%), maximum particle size (181.63 μm), widest particle size distribution, and highly non-uniformity (Figure 2A). Below the surface, sediments were dominated by silt, and the clay particle content increased and remained at about 10–13%. The phenomenon of coarse particles appeared again at 70.95 mbsf, different from the surface sediments, the particle size was more uniform. The particle size of the sediments at site W09 was relatively uniform, and the deep layers were better than

TABLE 2 Sequential extraction processes for studying the speciation of Fe in sediments.

Step	Extraction	Fe species	Fraction
1	1 mol L^{-1} Na-acetate brought to pH 4.5 with acetic acid for 24 h	Siderite ($FeCO_3$) and ankerite (Ca(Mg, Fe) $(CO_3)_2$)	Carbonate-associated
2	1 mol L^{-1} hydroxylamine-HCl for 48 h	Serrihydrite ($Fe_5HO_8\cdot4H_2O$) and lepidocrocite (γ-FeOOH)	Easily reducible (amorphous) oxides
3	Na-dithionite buffer brought to pH 4.8 with 0.30 mol L^{-1} acetic acid and 0.2 mol L^{-1} sodium citrate for 2 h	Goethite (α-FeOOH), hematite (α-Fe_2O_3), and akageneite (β-FeOOH)	Reducible (crystalline) oxides
4	0.2 mol L^{-1} ammonium oxalate and 0.17 mol L^{-1} oxalic acid solution for 6 h	Magnetite (Fe_3O_4)	Recalcitrant oxides
5	HNO_3, HCl, HF, and $HClO_4$	Mainly silicates	Residual

Summed by Poulton and Canfield (2005); Yang et al. (2018).

FIGURE 2
Sediment particle size analysis results of site W07 and W09. (A,B) show the particle size distribution, density distribution based on volume, and particle diameter calculated by the particle projection. (C) shows the textural classification of the samples based on Folk et al. (1970).
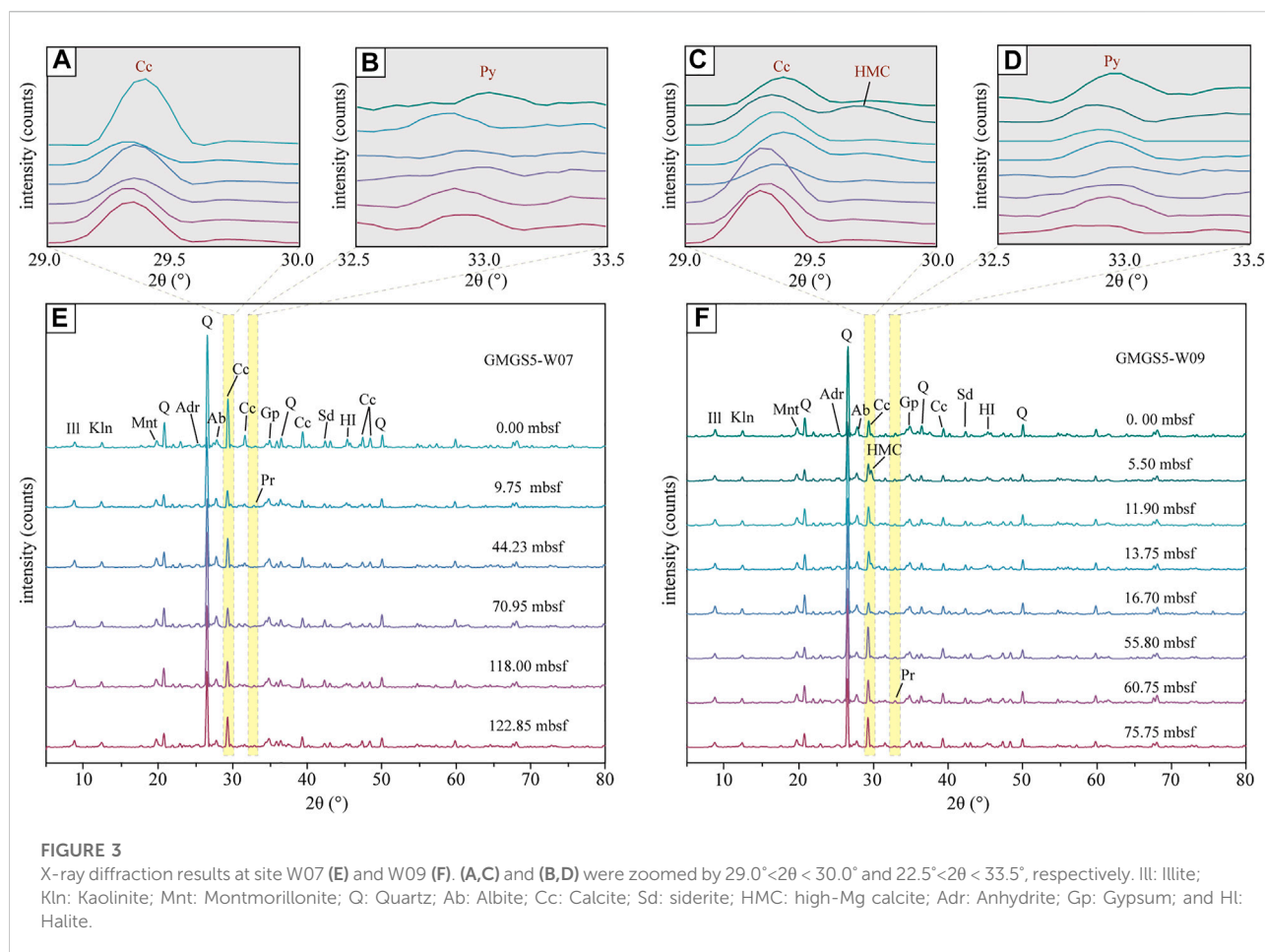
that of the shallow (Figure 2B). The silt content of site W09 was higher than 80%, and the sand content was always lower than that of silt and higher than that of clay at all sampling layers, but the sand content was significantly lower than that at site W07.

For ease of interpretation, the particle size of the sediments is generally separated into three fractions (Udden, 1914; He et al., 2009): clay (<4 μm), silt (4–63 μm), and sand (>63 μm), representing fine sediments, medium-sized sediments, and coarse sediments, respectively. Here, the sediment particle size triangle map projection was obtained using the method of Folk (Folk et al., 1970). As shown in Figure 2C, the particle size of site W07 was

concentrated in silt and sandy silt, and the cast points were relatively dispersed and roughly distributed in a linear shape. While sediment samples from site W09 had finer particles, all of which were silt, with concentrated cast points and better sorting.

4.2 Total organic carbon content

Sediment total organic carbon (TOC) contents of site W07 varied between 0.54% and 0.74%, with an average of 0.60%. The surface sediments on the seafloor had the highest TOC content

FIGURE 3
X-ray diffraction results at site W07 **(E)** and W09 **(F)**. **(A,C)** and **(B,D)** were zoomed by 29.0°<2θ < 30.0° and 22.5°<2θ < 33.5°, respectively. Ill: Illite; Kln: Kaolinite; Mnt: Montmorillonite; Q: Quartz; Ab: Albite; Cc: Calcite; Sd: siderite; HMC: high-Mg calcite; Adr: Anhydrite; Gp: Gypsum; and Hl: Halite.

of 0.74%, while the TOC contents of the remaining layers were less than 0.60%. Sediment TOC contents of site W09 varied between 0.50% and 0.58%, with an average of 0.54%. The peak of TOC appeared at 5.50 mbsf and 75.75 mbsf, respectively. On the whole, TOC contents of the sediments at the two sites were similar and varied little with depth.

## 4.3 Mineral composition and microscopic characteristics

The XRD patterns were quite similar at the two sites (Figure 3). There was a special assemblage of minerals at the two sites, which was characterized by clay minerals (illite and kaolinite), clastic rock minerals (quartz and albite), carbonate minerals (calcite and siderite), sulfate minerals (gypsum and anhydrite), and pyrite (Figures 3E,F). The characteristic peaks of quartz and calcite were strong in all layers, representing the main mineral phase in the sediments. The difference was that the clastic minerals of site W07 were higher, while site W09 had more clay minerals. To facilitate any comparisons in characteristic mineral content, we

chose calcite as a representative of carbonate and pyrite as a representative of sulfide, and the characteristic peaks of calcite (2θ = 29.30° ± 0.10°) and pyrite (2θ = 33.00° ± 0.10°) were zoomed in Figure 3. Zoomed-up insets showed the difference, and there was a clear peak of calcite in surface sediments and not varied significantly with depth at site W07, but the signal suddenly increased below 58.00 mbsf at site W09 (Figures 3A,C). Especially, an obvious characteristic peak can be observed at 2θ of 29.72° in the layer of 5.50 mbsf at site W09, which was identified as high-Mg calcite (Figure 3C). Looking back to pyrite, it seems to be more obvious in the surface layer than the deep, more obvious in site W09 than W07, with even no obvious characteristic peaks appearing in individual layers of site W07 (Figures 3B,D).

Under the scanning electron microscope, mineral crystals such as faces, corners, and edges were well-preserved (Figure 4), representing that those minerals were precipitated spontaneously and had not experienced transportation and abrasion. Among the observed authigenic carbonate minerals, calcite showed a relatively high content with mostly granulate, and aragonite had a needle-like shape (Figure 4). Moreover, some microalgae shells were also observed under the FESEM, like coccolithophores (Figure 4).
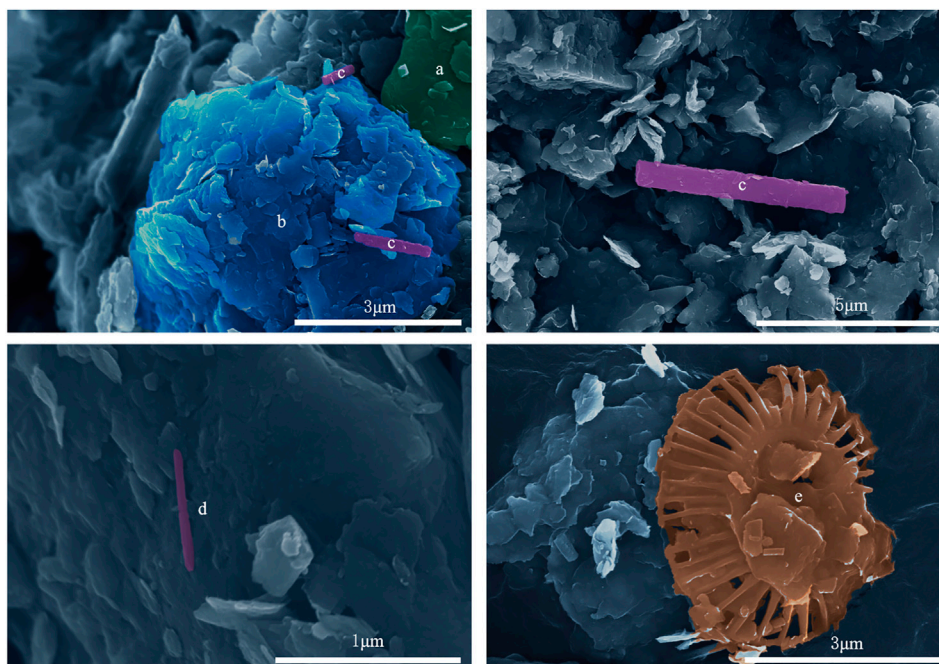
FIGURE 4
Typical samples under FESEM. **(A)** granular calcite; **(B)** flaky clay mineral; **(C)** columnar aragonite; **(D)** acicular aragonite; and **(E)** shell of coccolithophore.
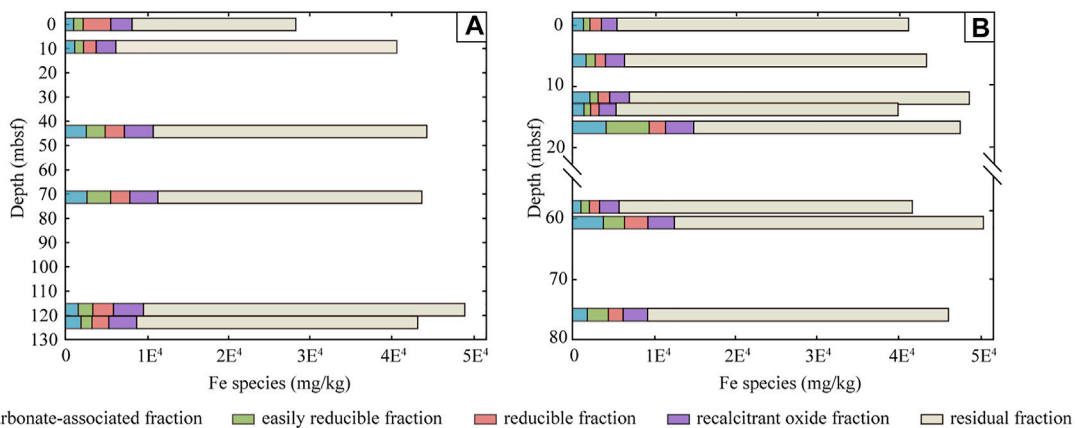
FIGURE 5
Mass accumulation of Fe species in sediments of site W07 **(A)** and W09 **(B)**.

4.4 Iron content and its chemical species

Through step-by-step extraction, the total amount of Fe (Fe_T) in the samples of the two sites and the proportions of Fe species were obtained. After calculating the recovery rate (the ratio of Fe_T proportions of different Fe species to the Fe_T), the results were all between 80 and 120%, which were judged to be the valid data (Poulton and Canfield, 2005; Larner et al., 2006; Claff et al., 2010).

4.4.1 Total iron content

Fe_T of the sediment samples at site W07 varied between 2.8 and 4.1 wt%, with the surface content being the lowest and

showing an increasing trend with depth. There was a peak at 44.23 mbsf, and then the second peak appears at 118.00 mbsf (Figure 5). The Fe_T of sediment samples from site W09 varied more complicatedly with depth, fluctuating between 3.8 and 4.5 wt%, with a relatively higher content occurring in 5.50, 16.70, and 60.75 mbsf (Figure 5). Overall, the Fe_T at site W09 was characterized by a high overall content and concentrated distribution compared to site W07.

4.4.2 Chemical species of iron

As can be seen from Figure 5, the concentrations of different forms of iron at site W07 were 1,009–2,651 mg/kg (equivalent to 3.1%–7.2% of total iron content) in the carbonate-associated fraction (siderite and ankerite), 1,085–2,870 mg/kg (3.0%–7.8%) in the easily reducible fraction (amorphous oxides: ferrihydrite and lepidocrocite), 1,553–3,353 mg/kg (4.3%–12.2%) in the reducible fraction (crystalline oxides: goethite, hematite, and akageneite), 2,378–3,649 mg/kg (6.6%–9.5%) in the recalcitrant oxide fraction (magnetite), and 19,970–39,206 mg/kg (72.6%–94.6%) in the residual fraction (mainly silicates).

The concentrations of different forms of iron at site W09 were 1,046–4,123 mg/kg (2.7%–9.2%) in the carbonate-associated fraction (siderite and ankerite), 798–5,284 mg/kg (2.0%–11.8%) in the easily reducible fraction (amorphous oxides: ferrihydrite and lepidocrocite), 1,044–2,871 mg/kg (2.8%–6.6%) in the reducible fraction (crystalline oxides: goethite, hematite, and akageneite), 1,902–3,482 mg/kg (4%–7.8%) in the recalcitrant oxide fraction (magnetite), and 32,658–41,684 mg/kg (72.9%–99.0%) in the residual fraction (mainly silicates).

Among the deposit forms of iron in the sediments at the two sites, there was no obvious advantage in the proportion of iron in different forms (except residual fraction). Specifically, the proportions of reducible fraction and recalcitrant oxide at site W07 were higher, while iron in site W09 was dominated by a carbonate-associated fraction and easily reducible fraction (Figure 5).

5 Discussion

5.1 Geochemical conditions for gas hydrate accumulation

5.1.1 Reservoir sediment matrix

Sediment particle size is a vital controlling factor for gas hydrates to store in reservoirs. It is undeniable that particle size generally decreases with the pore size, and the sediment permeability decreases with decreasing pore size (Vargas-Cordero et al., 2020). Consequently, the enrichment of gas hydrates in previous studies often showed the relationship corresponding to the layers with coarse-grained sediments and high sand content (Lu et al., 2011; Jinhua et al., 2018).

Different from the previous understanding, the results in this article show that gas hydrates are stored in fine-grained sediments, mainly silts, at site W07 and W09 (Figure 2C), indicating that the deposition environment is low-energy and relatively stable. The phenomenon of high-content gas hydrate exists in primarily fine-grained sediments also present in the SCS, specifically, sand content of the sediment hydrate accumulated in SSA is less than 10%, while the hydrate saturation is as high as 10–45% (Wang et al., 2010). In addition, recent studies have pointed out that agglomerates consisting of clay and silt particle may increase the apparent particle size and pore throat size of the sediments, preventing the relative permeability drop, and ultimately promoting gas hydrate growth in silt-rich sediments (Vargas-Cordero et al., 2020). The fine-grained particle restricts the pore spaces for gas hydrate growth, and at the same time, under the connection of structural fractures, massive gas hydrates with a vein-like or the disseminated structure have been formed in the boreholes in the study area (Liang et al., 2019). In addition, relatively coarse-grained particles are contained in the sediments at site W07 (Figures 2A,C), which may be the result of gas escape.

It is noteworthy that many coccolithophore shells can be observed under FESEM in the sediments (Figure 4) of the study sites. Layers with gas hydrate exhibit a positive feedback relationship with foraminifera and coccolithophore shells are common in SCS, such as the GMGS3 drilling area (Zhang et al., 2017) and site SH7B in SSA (Chen et al., 2013). In our study area, the appearance of coccolithophore shells increases the content of coarse-grained particles and the porosity of the sediments, which will provide more space for the formation and occurrence of gas hydrates.

5.1.2 Mineral compositions of reservoir sediments

The main mineral composition is expectedly similar in two different settings, and the change of mineral facies is not obvious with depth (Figures 3E,F). Influenced by gas hydrate environment, these minerals are largely authigenic with intact crystal forms (Figure 4).

As the direct product of AOM, authigenic carbonates deposit since a high concentration of HCO_3^- (Moore et al., 2004; Feng and Chen, 2015). Gas hydrate concentration at site W09 continued to increase with depth (Figure 1C), alkalinity driven by strong AOM promoted the process of combining Ca^{2+} and CO_3^{2-} to generate authigenic carbonate. Consequently, the content of calcite increased in the bottom layers (Figure 3C). Site W07 has a low and stable gas hydrate concentration, so it does not cause a significant variation of carbonate content in depth (Figure 3A). Yet, there is no obvious reason for a strong calcite signal in surface sediments at site W07, so it is speculated that calcite may not be self-generating. Otherwise, needle-like aragonites are often found in gas hydrate environments (Tong et al., 2013), which provides vital evidence for microbial activities associated with gas hydrates in the study area.

Pyrite is produced by combining with hydrogen sulfide generated in the geochemical process of gas hydrates environment (Schulz and Zabel, 2006). Compared with siderite, pyrite is a product of sulfate reduction, and consequently, related to a more reducing and acidic environment to some extent (Yang et al., 2018). The XRD analysis shows that the response of pyrite in all sediment samples is very weak, but the emergence of more pyrite under XRD in site W09 may correspond to its richer gas hydrate and more reducing sedimentary environment (Figures 3B,D). Apart from that, the presence of sulfate minerals, such as gypsum, in the study area indicates depositional environments with high sulfate contents.

5.1.3 Redox conditions of reservoir sediments

Natural gas hydrates that exist under seafloor are most commonly formed from microbial methane, so methanogenesis from sedimentary organic carbon plays a critical role in gas hydrate formation (Kvenvolden, 1993; Kvenvolden, 1995). Studies have shown that gas is generated if the average sediment organic carbon content is greater than 0.5% (Waseda, 1998), and probably 75% of the gas hydrates accumulate within the area with sediments containing >0.5% TOC content (Harvey and Huang, 1995). In contrast, sediments at site W07 have higher TOC contents (TOC_{W07} = 0.60%, TOC_{W09} = 0.54%), suggesting better gas production capacity and may lead to more free gas in sediments.

5.2 Geochemical behaviors of elements

5.2.1 Migration and transformation of iron

Dissolution, precipitation, and transformation of Fe-minerals are dynamic in response to alternating redox conditions in marine sediments, which is one of the key active elements in the ocean (Froelich et al., 1979; Klinkhammer et al., 1982; Nevin and Lovley, 2002; Lyons and Severmann, 2006). Dynamic changes in methane fluid and multistage gas hydrate evolution change the geochemistry conditions, thereby causing the migration and transformation of Fe in the study area. Sequential extraction experiments show important differences in Fe_T and different forms of Fe-minerals among the methane-rich layer and its adjacent layer, indicating that significant Fe migration and transformation have occurred (Figure 6).

For better explanation, here, we think that Fe (II)-containing minerals are concentrated in the first step extracts, and Fe in other extractions is defined as Fe (III)-containing minerals. It is noteworthy that an obvious increase in Fe (II)-containing minerals have occurred in 11.90, 16.70, and 60.75 mbsf at site W09, where enormous gas hydrates (nodular, vein-like, and fracture-filling hydrate) or hydrate dismission appeared (Figure 6). In addition, in site W07, the phenomenon of the Fe (II)-containing minerals increased at 44.23 and 70.95 mbsf,
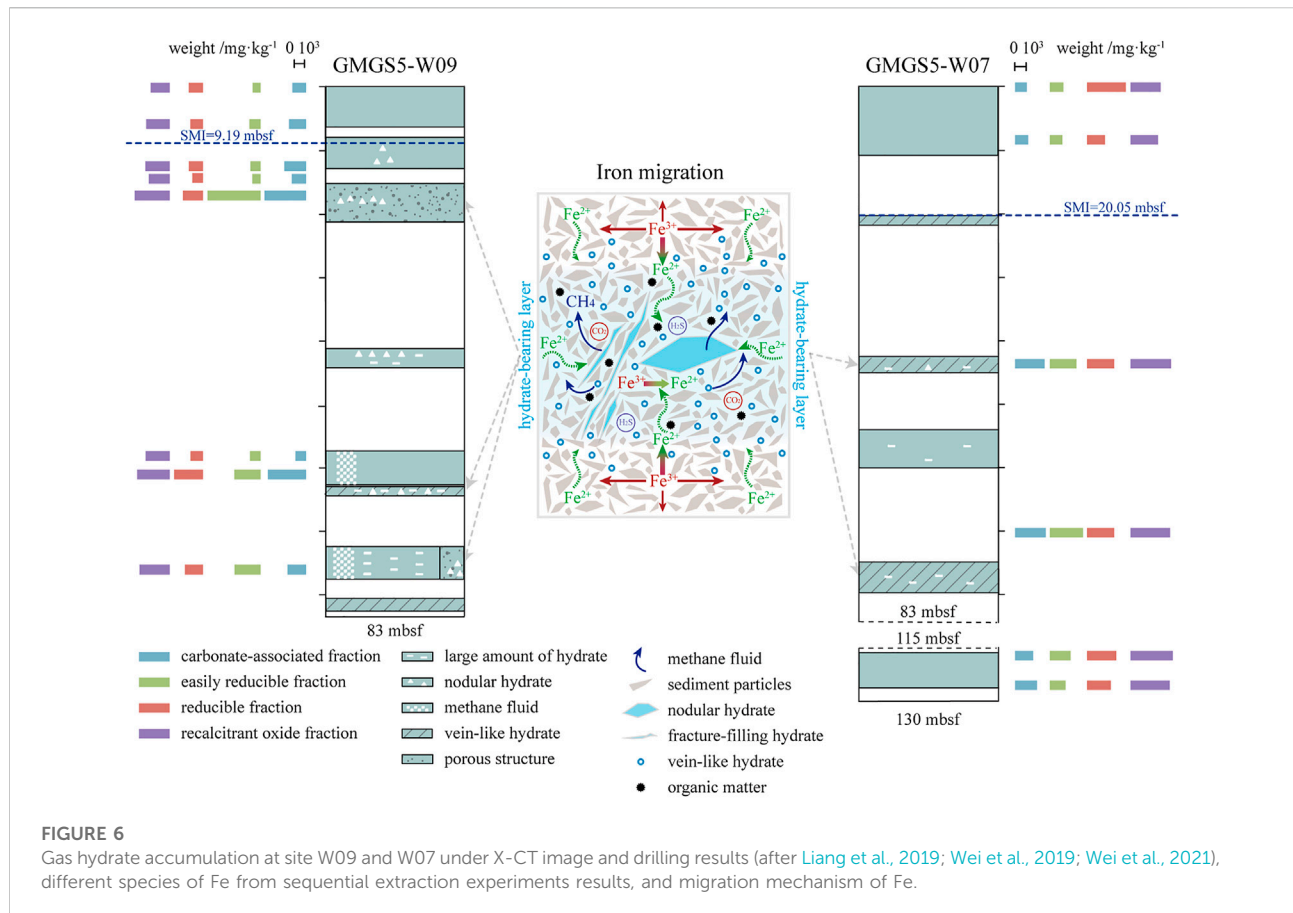
where vein-like hydrate and enormous hydrate occurred (Figure 6). Interestingly, enrichment of Fe occurred in these methane-rich layers, which is similar to the proportion of Fe (II). In sum, the abovementioned results can be summarized as two important phenomena: 1) The Fe_T in methane-rich layers increased, conversely, decreased in the adjacent layers; 2) Suddenly an increase of Fe(II)-containing minerals appeared in methane-rich layers. The explanation of these two phenomena can be divided into two parts: dissolution and precipitation during Fe migration, which is discussed, respectively, in the following two paragraphs.

The residual fraction (mainly silicates) did not seem to be the main source of dissolved Fe, although it occupies the main ingredient of Fe in all sediment samples. There is a phenomenon that the Fe_T of the methane-rich layer is higher, but the residual fraction content is lower than that of the adjacent layers, such as 16.70 mbsf at site W09. In addition, the dissolved amount is not enough to provide so much Fe to participate in migration, like 60.75 mbsf at site W09. In this way, the remaining species should be the main contributor to migration, and while the dissolved components may not be specific, but all does contribute.

The concentrated precipitation of Fe-minerals in the gas hydrate-bearing environment is related to the oxidation of methane that promotes environmental reducibility. The presence of methane, carbon dioxide, and hydrogen sulfide are characteristics of the gas hydrate-bearing environment, especially when seepage have occurred (Dando et al., 1999; Pape et al., 2008). Geochemical conditions near the methane-rich layers are biased toward reducing along with the process of AOM, causing the Fe-minerals to dissolve into the pore water and gradually migrate to the methane-rich layer (e.g., Hensen et al., 2003; März et al., 2008; Yang et al., 2018). In the methane-rich layer, Fe^{3+} is reduced and the surrounding Fe^{2+} (original and reduced from Fe^{3+}) is "attracted" and "captured" at the same time (Figure 6). Ultimately, the migration and transformation process will be initiated with these aggregated Fe ions precipitating in the form of minerals. Although Fe (III)-containing minerals are more stable, the reducibility of the environment and the increase of Fe^{2+} promote the increase of Fe(II)-containing minerals precipitation. Therefore, the increase of Fe(II)-containing minerals, rather than Fe (III)-containing minerals, are more evident in all deposited Fe-minerals.

5.2.2 Enrichment of redox-sensitive trace elements

The proportion of trace elements in marine sediments may be affected by various factors, and untreated content-change of trace elements would obscure important geological information (Tribovillard et al., 2006). Compared with other elements, Al in sediments has stable and conservative physical and chemical properties, which is always used as a normalization element (Brumsack, 1989; Morford and Emerson, 1999). Usually, after Al

FIGURE 6
Gas hydrate accumulation at site W09 and W07 under X-CT image and drilling results (after Liang et al., 2019; Wei et al., 2019; Wei et al., 2021), different species of Fe from sequential extraction experiments results, and migration mechanism of Fe.

standardization, the influence of terrestrial inputs and biogenic diluents (calcium carbonate and opal) in marine sediments could be eliminated. Moreover, to better interpret the standardization results, it is customary to use enrichment factors (EF): $EF_{element}$ X = $X/Al_{sample}/X/Al_{average}$ (Tribovillard et al., 2006). Element X is enriched relative to the average upper curst when $EF_X > 1$, and it is depleted when $EF_X < 1$. If $EF_X > 10$, it represents very rich X (Tribovillard et al., 2006; Algeo and Tribovillard, 2009). The Earth's upper crust compositions (McLennan, 2001) were used to calculate $X/Al_{average}$ in this article, and the enrichment factor analysis of the elements in the sediment samples of site W07 and W09 were presented in Table 3.

To correlate intercorrelations between trace elements and TOC, Pearson correlation analysis was performed. Correlation coefficients with absolute values greater than 0.6 were considered strongly correlated, which were highlighted in bold fonts in Table 4 and Table 5.

The results demonstrate that EFs of Co, Ni, Cu, Zn, Fe, Mn, and Ba are slightly higher than the Earth's upper crust, which suggests null to minor enrichment (Figure 7). In previous studies, no obvious enrichment of these trace elements in gas hydrate-bearing sediments of SCS were also found (Deng et al., 2017; Lin et al., 2022). Redox-sensitive elements like Co, Ni, Cu, and Zn

are sensitive to hypoxic environment and organic matter (Morford and Emerson, 1999; Tribovillard et al., 2006), and these elements show that the degree of enrichment slightly increases in methane-rich layers of the two sites (Figure 7). The results of Pearson correlation analysis show that Co, Ni, Cu, and Zn are not proportional to TOC, but have a strong and significant correlation with Fe and Mn (Table 4, 5). This result illustrates that Fe- and Mn-dependent oxidation (of methane) may dominate the enrichment of trace elements in these two sites. Ba_{EF} in marine sediments can be used as an effective indicator for marine paleoproductivity (Dymond et al., 1992). Since the positive correlation between Ba and TOC content is not very strong (Table 4, 5), it is still possible that a part of Ba is carried by the upwelling of methane fluxes from gas hydrate decomposition. The relationship between Fe, Mn, and TOC contents shows a weak–moderate negative correlation (Table 4, 5), which means that organic matter is not a source of Fe and Mn. The difference is that the correlations of Fe and Mn with Ba of the two sites are diametrically opposite. Therefore, the positive correlations of Fe and Mn with Ba at site W07 is the result of the influence of methane seepage to a large extent. Conversely, the negative correlations of Fe and Mn with Ba at site W09 suggests that elements are likely to be from other sources, such as the direct precipitation of seawater.

TABLE 3 Enrichment factors for trace elements and TOC% of sediments.

Samples	Mo$_{EF}$	V$_{EF}$	Co$_{EF}$	Ni$_{EF}$	Cu$_{EF}$	Zn$_{EF}$	Cr$_{EF}$	As$_{EF}$	Sb$_{EF}$	Fe$_{EF}$	Mn$_{EF}$	Ba$_{EF}$	TOC %
W07B-1	6.22	0.94	1.17	1.39	1.38	2.42	1.47	67.20	233.08	0.93	4.76	1.62	0.74
W07B-2	3.78	0.86	0.92	0.81	0.75	1.52	1.23	53.79	178.83	0.89	0.99	0.76	0.58
W07B-3	2.02	1.07	1.20	1.12	1.21	1.93	1.51	51.60	127.55	1.10	1.28	0.94	0.6
W07B-4	4.36	0.75	0.87	0.68	1.13	1.36	1.07	56.45	199.64	0.73	0.95	0.67	0.58
W07B-5	5.02	1.10	1.16	1.23	1.04	2.23	1.41	56.84	190.16	1.07	1.19	0.72	0.54
W07B-6	2.48	1.17	1.15	1.07	1.40	2.22	1.47	61.73	195.43	1.09	1.11	0.81	0.58
W09B-1	3.70	1.26	1.44	1.27	1.15	2.22	1.84	60.26	149.73	1.32	1.39	0.89	0.55
W09B-2	19.51	1.23	1.39	1.33	1.36	2.10	1.61	60.58	130.91	1.29	1.42	0.98	0.52
W09B-3	1.11	1.26	1.50	1.28	1.24	2.23	1.70	61.53	121.58	1.35	1.53	0.93	0.57
W09B-4	1.69	1.02	1.16	1.01	0.95	1.91	1.47	57.77	121.62	1.09	1.17	0.80	0.54
W09B-5	0.38	1.37	1.62	1.33	1.31	2.35	1.89	58.92	101.32	1.51	1.90	1.01	0.52
W09B-6	3.01	1.72	1.86	1.74	1.90	2.81	2.31	73.77	229.58	1.71	1.87	0.98	0.52
W09B-7	1.58	1.35	1.57	1.34	1.21	2.70	1.88	62.90	154.29	1.47	1.70	1.06	0.51
W09B-8	1.96	1.05	1.24	1.39	1.33	2.13	1.41	58.18	122.58	1.17	1.12	3.47	0.58
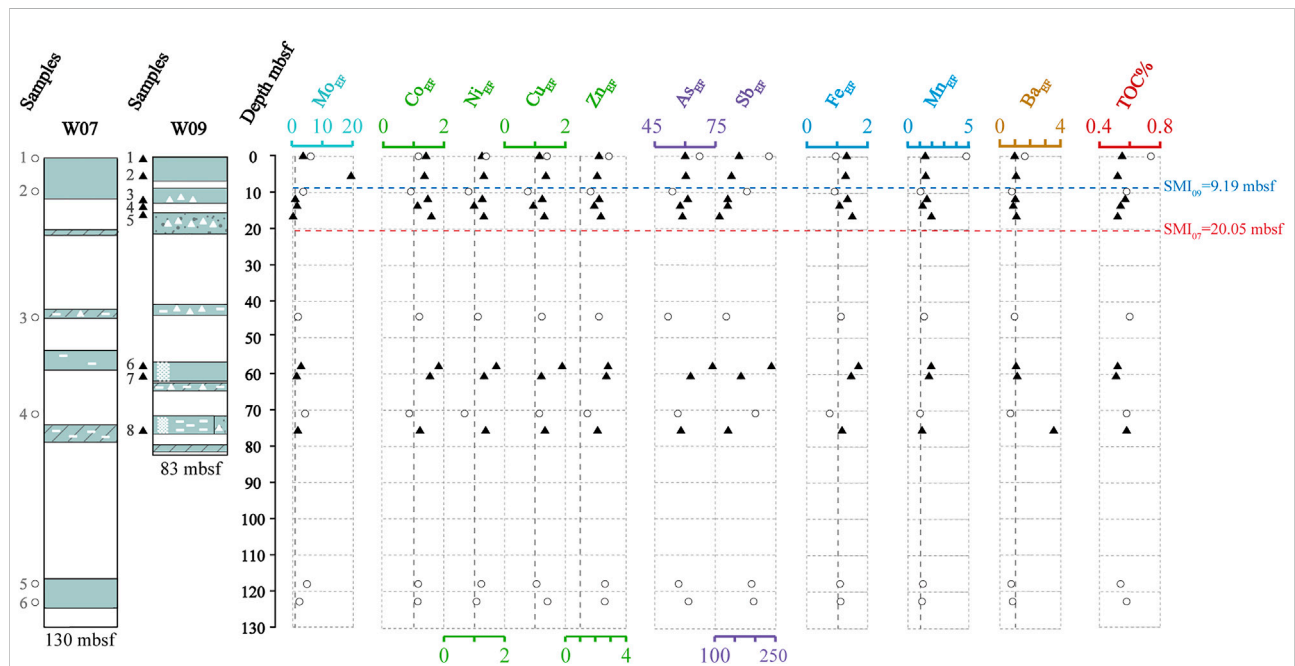
FIGURE 7
TOC% and enrichment factors of Mo (Mo$_{EF}$), Co (Co$_{EF}$), Ni (Ni$_{EF}$), Cu (Cu$_{EF}$), Zn (Zn$_{EF}$), As (As$_{EF}$), Sb (Sb$_{EF}$), Fe (Fe$_{EF}$), Mn (Mn$_{EF}$), and Ba (Ba$_{EF}$) in the sediment profile at site W07 and site W09. The enrichment factor (EF) was calculated as X$_{EF}$ = [(X/Al)$_{sample}$/(X/Al)$_{average}$], and the samples were normalized using Earth's upper crust compositions (McLennan, 2001).

Mo shows a minor to moderate enrichment in sediments (Figure 7). The anomalously enriched Mo in many studies is interpreted as H$_2$S generated by the AOM during the seepage, which accumulates on the top of the sediment profile, and even seeps out into the seawater (Hu et al., 2014; Chen et al., 2016; Li C. et al., 2016; Liu et al., 2020). Since Mo is easily migrated and enriched in the deposition environment containing hydrogen sulfide, which often occurs in environments with intense methane seepage and strong AOM near SMTZ (Peketi et al., 2012; Hu et al., 2015b; Deng et al., 2017), this may have interfered

TABLE 4 Results of Pearson correlation analysis of site GMGS5-W07.

	Mo_{EF}	V_{EF}	Co_{EF}	Ni_{EF}	Cu_{EF}	Zn_{EF}	Cr_{EF}	As_{EF}	Sb_{EF}	Fe_{EF}	Mn_{EF}	Ba_{EF}	TOC %
Mo_{EF}	1	−0.44	−0.46	−0.19	−0.53	−0.22	−0.58	0.09	**0.64**	−0.46	−0.44	**−0.88**	**−0.81**
V_{EF}		1	**0.95**	**0.91**	0.56	**0.97**	**0.95**	0.35	−0.24	**0.97**	**0.79**	0.56	−0.16
Co_{EF}			1	**0.95**	0.54	**0.91**	**0.97**	0.093	−0.47	**0.97**	**0.94**	**0.68**	−0.066
Ni_{EF}				1	0.34	**0.94**	**0.90**	0.096	−0.34	**0.94**	**0.89**	0.49	−0.36
Cu_{EF}					1	0.52	0.48	0.53	−0.031	0.41	0.41	0.34	0.23
Zn_{EF}						1	**0.87**	0.43	−0.064	**0.92**	**0.74**	0.37	−0.38
Cr_{EF}							1	0.06	−0.53	**0.99**	**0.90**	**0.77**	0.036
As_{EF}								1	**0.76**	0.11	−0.23	−0.39	−0.36
Sb_{EF}									1	−0.43	**−0.69**	**−0.89**	−0.58
Fe_{EF}										1	**0.87**	**0.68**	−0.11
Mn_{EF}											1	**0.75**	0.0078
Ba_{EF}												1	**0.62**
TOC %													1

Bold fonts represent strong correlation (the absolute value of Pearson coefficient is greater than 0.6).

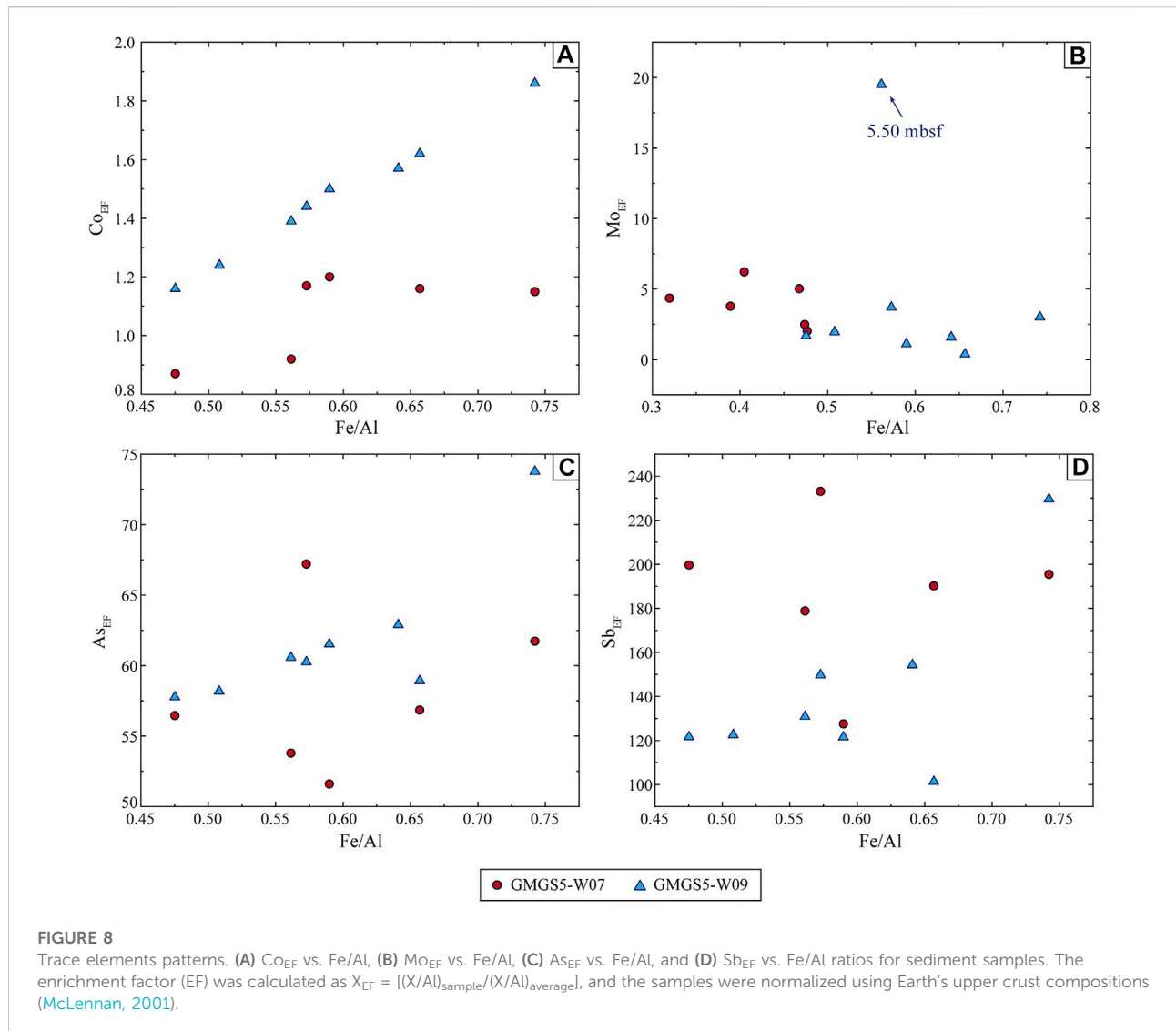TABLE 5 Results of Pearson correlation analysis of site GMGS5-W09.

	Mo_{EF}	V_{EF}	Co_{EF}	Ni_{EF}	Cu_{EF}	Zn_{EF}	Cr_{EF}	As_{EF}	Sb_{EF}	Fe_{EF}	Mn_{EF}	Ba_{EF}	TOC %
Mo_{EF}	1	−0.068	−0.14	0.034	0.12	−0.24	−0.17	−0.025	0.0041	−0.14	−0.17	−0.14	−0.28
V_{EF}		1	**0.98**	**0.83**	**0.84**	**0.89**	**0.99**	**0.90**	**0.78**	**0.98**	**0.88**	−0.39	−0.55
Co_{EF}			1	**0.79**	**0.78**	**0.90**	**0.98**	**0.82**	**0.67**	**1.00**	**0.93**	−0.38	−0.52
Ni_{EF}				1	**0.98**	**0.78**	**0.77**	**0.84**	**0.78**	**0.79**	0.56	0.14	−0.20
Cu_{EF}					1	**0.69**	**0.77**	**0.87**	**0.80**	**0.77**	0.54	0.0046	−0.22
Zn_{EF}						1	**0.9**	**0.81**	**0.75**	**0.92**	**0.79**	−0.20	−0.51
Cr_{EF}							1	**0.88**	**0.76**	**0.98**	**0.90**	−0.44	−0.59
As_{EF}								1	**0.96**	**0.81**	**0.60**	−0.27	−0.37
Sb_{EF}									1	**0.67**	0.41	−0.16	−0.36
Fe_{EF}										1	**0.94**	−0.37	−0.56
Mn_{EF}											1	−0.53	**−0.65**
Ba_{EF}												1	**0.65**
TOC %													1

Bold fonts represent strong correlation (the absolute value of Pearson coefficient is greater than 0.6).

with the relationship between Mo and other trace elements in the study area (Table 4, 5). Recently, mild to extreme enrichment of Mo were recognized in gas hydrate- or seepage-impact anoxic sediments of the SCS (Chen et al., 2016; Deng et al., 2017; Lin et al., 2022). In our study, it can be seen that Mo_{EF} is only moderately enriched in sample W09B-2 (Mo_{EF} = 19.51), indicating the SMI below it (Figure 7). It is also understandable that the enrichment of Mo is not evident in deep sediments, where the AOM process is not as strong as near SMTZ. A convincing mechanism to explain the distribution of Mo, As, and Sb is the so-called particulate shuttle process, which illustrates that these elements will be scavenged by Fe- and Mn-oxyhydroxides in the water column (Tribovillard et al., 2006; Scott and Lyons, 2012; Tribovillard et al., 2013). Except derived

from the seawater, seep fluid is a plausible additional source of Fe, Mo, As, and Sb (Nath et al., 2008; Cangemi et al., 2010). It seems that the particulate shuttle process is unfeasible because there is no favorable relationship between Mo_{EF} and Fe/Al (Figure 8), but additional input of seep fluids may play a critical role.

As and Sb are of special interest as they are extremely enriched in sediments (Figure 7). In fact, the phenomenon of anomalous enrichment of As and Sb in gas hydrate accumulation area is relatively recent, and the most likely reason may be affected by authigenic Fe fraction (Nath et al., 2008; Hu et al., 2014). The enrichment factor of As exceeds 60, while the content of Sb is even higher in our study, which is around 200-fold higher than the average value. Significant enrichments of As and Sb also appeared in the hydrocarbon seeps of the Niger Delta margin, but

FIGURE 8
Trace elements patterns. **(A)** Co_{EF} vs. Fe/Al, **(B)** Mo_{EF} vs. Fe/Al, **(C)** As_{EF} vs. Fe/Al, and **(D)** Sb_{EF} vs. Fe/Al ratios for sediment samples. The enrichment factor (EF) was calculated as $X_{EF} = [(X/Al)_{sample}/(X/Al)_{average}]$, and the samples were normalized using Earth's upper crust compositions (McLennan, 2001).

moderate enrichments were more common in the seep areas of the SCS (Hu et al., 2014; Lin et al., 2022). As mentioned in chapter 5.2.1, Fe(III)–Fe(II) transition undergoes in the gas hydrate-bearing layers under hypoxic conditions. This process will release trace elements (e.g., As and Sb) and eventually lead to an increase in the EFs. In particular, positively and highly correlations between As, Sb, and Fe/Al are found in site W09 (Figure 8), confirming that the cycle of Fe-oxyhydroxides should be involved in the adsorption and release of As and Sb. Also, high contents of As and Sb in study sediments suggest the availability of abundant dissolved As and Sb during Fe-oxyhydroxides formation. However, the relationship between As, Sb, and Fe/Al in site W07 is not obvious (Figure 8), which is presumed to have received additional ascending fluids input.

5.2.3 Evidence of seepages from Sr/Ca and Mg/Ca

The formation of gas hydrates may lead to a higher concentration of Mg^{2+} in the surrounding pore water, thereby inhibiting the crystallization of calcite and promoting the formation of aragonite (Berner, 1975). As a result, the formation of aragonite and high-Mg calcite can reflect methane seepage to a certain extent. Aragonite is formed in the period of high seepage or high methane flux, while high-Mg calcite is formed in the period of methane diffusion with low or no seepage (Bayon et al., 2007). In addition, the ratios of Sr/Ca and Mg/Ca can be used to identify aragonite (Sr-rich) and high-Mg calcite (Mg-rich) in methane seepage sediments (Bayon et al., 2007; Yang et al., 2014; Chen et al., 2016).
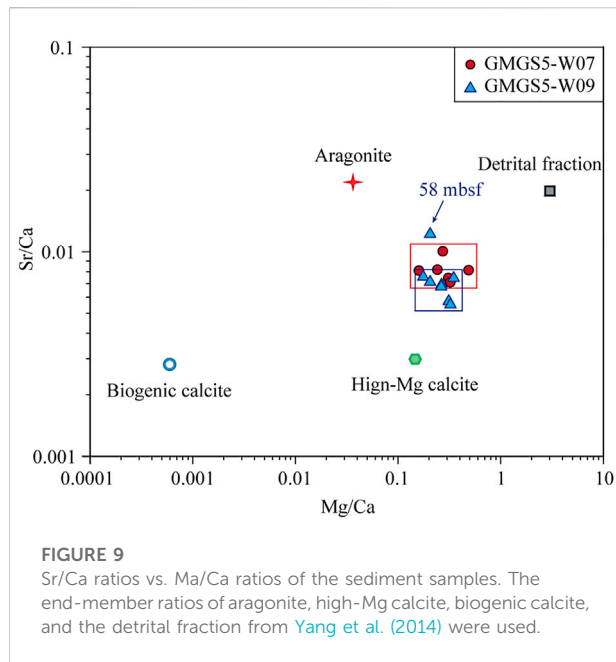
FIGURE 9
Sr/Ca ratios vs. Ma/Ca ratios of the sediment samples. The end-member ratios of aragonite, high-Mg calcite, biogenic calcite, and the detrital fraction from Yang et al. (2014) were used.

Figure 9 shows that the ratios of Sr/Ca and Mg/Ca in all sediments are more inclined to distribute along the direction of precipitation of the high-Mg calcite, suggesting that Sr/Ca and Mg/Ca in the sediments may mainly in the form of high-Mg calcite. Overall, it can be considered that methane seepage in site W07 and W09, at least at the shallow layers, are relatively weak (Figure 9). But it is worth noting that sediments at site W07 have higher Sr/Ca ratios, which may represent more active gas activity during the multistage gas hydrate evolution. Meanwhile, the characteristic peak of high-Mg calcite is only found in the sediments of site W09 (Figure 3C), which further confirms the seepage of site W09 is much weaker than site W07. But there is an exception in the layer of 58.00 mbsf at site W09, where seepage happened related to the present nearby high-concentration gas hydrates decomposition and lead to the Sr/Ca and Mg/Ca values of sediments being more inclined to aragonite (Figure 9).

6 Conclusion

In this study, the geochemical characteristics of sediments from sites GMGS5-W07 and GMGS5-W09 are investigated, and the following conclusions can be reached:

(1) Based on the physical and chemical characteristics of sediments, fine-grained sediments dominated by silt suggest a low-energy and relatively stable sedimentary environment, and the appearance of coccolithophore shells can provide more pore space for gas hydrate to form. TOC contents of sediments in both the sites are greater than 0.5%, suggesting sufficient gas availability for gas hydrate formation. Moreover, the appearances of authigenic carbonate minerals, sulfate minerals, and pyrite might be associated with the occurrence of gas hydrates in the sediments of the two sites.

(2) The reducing condition of gas hydrate-bearing sediments might be a significant factor of chemical species of Fe. The migration and chemical state transformation of Fe in sediments might be associated with gas hydrate occurrence. The methane-rich layer can convert Fe^{3+} to Fe^{2+} and capture authigenic iron carbonates in association with methane oxidation in an anoxic environment.

(3) Redox-sensitive elements in the sediments are mainly hosted by Fe- and Mn-oxyhydroxides, and the enrichment of Co, Ni, Cu, Zn, As, and Sb might be associated with the occurrence of massive gas hydrate. Mo, As, and Sb in the sediments of site W07 are likely to be additionally affected by deep methane fluids, while they are not observed at site W09. This finding suggests that geochemical behaviors of redox-sensitive elements are more affective to seep fluids than gas hydrate saturation in sediments.

Data availability statement

The raw data supporting the conclusion of this article will be made available by the authors, without undue reservation.

Author contributions

YL, HY, and HL conceived this study; YF and ZK supervised the investigation; YL and HY wrote the draft of the manuscript; and HL and YF revised the manuscript.

Funding

Acknowledgments

special issue, and reviewers for helping in refining the manuscript.

Conflict of interest

Publisher's note

References

Algeo, T. J., and Tribovillard, N. (2009). Environmental Analysis of Paleoceanographic Systems Based on Molybdenum–Uranium Covariation. *Chem. Geol.* 268, 211–225. doi:10.1016/j.chemgeo.2009.09.001

Bayon, G., Pierre, C., Etoubleau, J., Voisset, M., Cauquil, E., Marsset, T., et al. (2007). Sr/Ca and Mg/Ca Ratios in Niger Delta Sediments: Implications for Authigenic Carbonate Genesis in Cold Seep Environments. *Mar. Geol.* 241, 93–109. doi:10.1016/j.margeo.2007.03.007

Berner, R. A. (1975). The Role of Magnesium in the Crystal Growth of Calcite and Aragonite from Sea Water. *Geochimica Cosmochimica Acta* 39, 489–504. doi:10.1016/0016-7037(75)90102-7

Boetius, A., Ravenschlag, K., Schubert, C. J., Rickert, D., Widdel, F., Gieseke, A., et al. (2000). A Marine Microbial Consortium Apparently Mediating Anaerobic Oxidation of Methane. *Nature* 407, 623–626. doi:10.1038/35036572

Boetius, A., and Wenzhöfer, F. (2013). Seafloor Oxygen Consumption Fuelled by Methane from Cold Seeps. *Nat. Geosci.* 6, 725–734. doi:10.1038/ngeo1926

Borowski, W. S., Paull, C. K., and Ussler, I. (1996). Marine Pore-Water Sulfate Profiles Indicate *In Situ* Methane Flux from Underlying Gas Hydrate. *Geol.* 24, 655–658. doi:10.1130/0091-7613(1996)024<0655:mpwspi>2.3.co;2

Boswell, R. (2007). Exploration Priorities for Marine Gas Hydrate Resources. *Fire Ice 2007 Spring/Summer*, 11–13.

Brumsack, H. (1989). Geochemistry of Recent TOC-Rich Sediments from the Gulf of California and the Black Sea. *Geol. Rundsch.* 78, 851–882. doi:10.1007/bf01829327

Cangemi, M., Di Leonardo, R., Bellanca, A., Cundy, A., Neri, R., and Angelone, M. (2010). Geochemistry and Mineralogy of Sediments and Authigenic Carbonates from the Malta Plateau, Strait of Sicily (Central Mediterranean): Relationships with Mud/fluid Release from a Mud Volcano System. *Chem. Geol.* 276, 294–308. doi:10.1016/j.chemgeo.2010.06.014

Chen, F., Hu, Y., Feng, D., Zhang, X., Cheng, S., Cao, J., et al. (2016). Evidence of Intense Methane Seepages from Molybdenum Enrichments in Gas Hydrate-Bearing Sediments of the Northern South China Sea. *Chem. Geol.* 443, 173–181. doi:10.1016/j.chemgeo.2016.09.029

Chen, F., Su, X., Lu, H. F., Zhou, Y., and Zhuang, C. (2013). Relations between Biogenic Component (Foraminifera) and Highly Saturated Gas Hydrates Distribution from Shenhu Area, Northern South China Sea. *Earth Science–Journal China Univ. Geosciences* 38, 907–915.

Claff, S. R. S. C., Sullivan, L. A., Burton, E. D., and Bush, R. T. (2010). A Sequential Extraction Procedure for Acid Sulfate Soils: Partitioning of Iron. *Geoderma* 155, 224–230. doi:10.1016/j.geoderma.2009.12.002

Collett, T. S., Bird, K. J., Kvenvolden, K. A., and Magoon, L. B. (1988). Geologic Interrelations Relative to Gas Hydrates within the North Slope of Alaska. *U. S. Geol. Surv. Open-File Rep.* 88, 150.

Cui, H., Su, X., Chen, F., Holland, M., Yang, S., Liang, J., et al. (2019). Microbial Diversity of Two Cold Seep Systems in Gas Hydrate-Bearing Sediments in the South China Sea. *Mar. Environ. Res.* 144, 230–239. doi:10.1016/j.marenvres.2019.01.009

Dando, P. R., Stüben, D., and Varnavas, S. P. (1999). Hydrothermalism in the Mediterranean Sea. *Prog. Oceanogr.* 44, 333–367. doi:10.1016/s0079-6611(99)00032-4

Deng, Y., Fang, Y., Zhang, X., Chen, F., Wang, H., Ren, J., et al. (2017). Trace Element Geochemistry of Sediments in Qiongdongnan Area, the South China Sea, and its Implications for Gas Hydrates. *Mar. Geol. Quat. Geol.* 37, 70–81.

Devol, A. H., and Ahmed, S. I. (1981). Are High Rates of Sulphate Reduction Associated with Anaerobic Oxidation of Methane? *Nature* 291, 407–408. doi:10.1038/291407a0

Dymond, J., Suess, E., and Lyle, M. (1992). Barium in Deep-Sea Sediment: A Geochemical Proxy for Paleoproductivity. *Paleoceanography* 7, 163–181. doi:10.1029/92pa00181

Egawa, K. K. E. I., Nishimura, O., Izumi, S., Fukami, E., Jin, Y., Kida, M., et al. (2015). Bulk Sediment Mineralogy of Gas Hydrate Reservoir at the East Nankai Offshore Production Test Site. *Mar. Pet. Geol.* 66, 379–387. doi:10.1016/j.marpetgeo.2015.02.039

Fang, Y., Wei, J., Lu, H., Liang, J., Lu, J., Fu, J., et al. (2019). Chemical and Structural Characteristics of Gas Hydrates from the Haima Cold Seeps in the Qiongdongnan Basin of the South China Sea. *J. Asian Earth Sci.* 182, 103924. doi:10.1016/j.jseaes.2019.103924

Feng, D., and Chen, D. (2015). Authigenic Carbonates from an Active Cold Seep of the Northern South China Sea: New Insights into Fluid Sources and Past Seepage Activity. *Deep Sea Res. Part II Top. Stud. Oceanogr.* 122, 74–83. doi:10.1016/j.dsr2.2015.02.003

Fischer, D., Mogollón, J. M., Strasser, M., Pape, T., Bohrmann, G., Fekete, N., et al. (2013). Subduction Zone Earthquake as Potential Trigger of Submarine Hydrocarbon Seepage. *Nat. Geosci.* 6, 647–651. doi:10.1038/ngeo1886

Folk, R. L., Andrews, P. B., and Lewis, D. W. (1970). Detrital Sedimentary Rock Classification and Nomenclature for Use in New Zealand. *N. Z. J. Geol. Geophys.* 13, 937–968. doi:10.1080/00288306.1970.10418211

Froelich, P. N., Klinkhammer, G. P., Bender, M. L., Luedtke, N. A., Heath, G. R., Cullen, D., et al. (1979). Early Oxidation of Organic Matter in Pelagic Sediments of the Eastern Equatorial Atlantic: Suboxic Diagenesis. *Geochimica Cosmochimica Acta* 43, 1075–1090. doi:10.1016/0016-7037(79)90095-4

Ginsburg, G., Soloviev, V., Matveeva, T., and Andreeva, I. (2000). 24. Sediment Grain-Size Control on Gas Hydrate Presence. *Sites* 994 (995), 997.Proc. of the Ocean Drilling Program, Scientific Results. 237-245.

Harvey, L. D., and Huang, Z. (1995). Evaluation of the Potential Impact of Methane Clathrate Destabilization on Future Global Warming. *J. Geophys. Res.* 100, 2905–2926. doi:10.1029/94jd02829

He, H., Chen, H., Yao, Q., Qin, Y., Mi, T., and Yu, Z. (2009). Behavior of Different Phosphorus Species in Suspended Particulate Matter in the Changjiang Estuary. *Chin. J. Ocean. Limnol.* 27, 859–868. doi:10.1007/s00343-009-9021-6

Hedrich, S., Schlömann, M., and Johnson, D. B. (2011). The Iron-Oxidizing Proteobacteria. *Microbiology* 157, 1551–1564. doi:10.1099/mic.0.045344-0

Hensen, C., Zabel, M., Pfeifer, K., Schwenk, T., Kasten, S., Riedinger, N., et al. (2003). Control of Sulfate Pore-Water Profiles by Sedimentary Events and the Significance of Anaerobic Oxidation of Methane for the Burial of Sulfur in Marine Sediments. *Geochimica Cosmochimica Acta* 67, 2631–2647. doi:10.1016/s0016-7037(03)00199-6

Himmler, T., Haley, B. A., Torres, M. E., Klinkhammer, G. P., Bohrmann, G., Peckmann, J., et al. (2013). Rare Earth element geochemistry in cold-seep pore waters of Hydrate Ridge, northeast Pacific Ocean. *Geo-Marine Letters.* 33, 369–379. doi:10.1007/s00367-013-0334-2

Hu, Y., Feng, D., Chen, L., Zheng, G., Peckmann, J., and Chen, D. (2015a). Using Iron Speciation in Authigenic Carbonates from Hydrocarbon Seeps to Trace Variable Redox Conditions. *Mar. Petroleum Geol.* 67, 111–119. doi:10.1016/j.marpetgeo.2015.05.001

Hu, Y., Feng, D., Liang, Q., Xia, Z., Chen, L., and Chen, D. (2015b). Impact of Anaerobic Oxidation of Methane on the Geochemical Cycle of Redox-Sensitive Elements at Cold-Seep Sites of the Northern South China Sea. *Deep Sea Res. Part II Top. Stud. Oceanogr.* 122, 84–94. doi:10.1016/j.dsr2.2015.06.012

Hu, Y., Feng, D., Peckmann, J., Roberts, H. H., and Chen, D. (2014). New Insights into Cerium Anomalies and Mechanisms of Trace Metal Enrichment in Authigenic

Carbonate from Hydrocarbon Seeps. *Chem. Geol.* 381, 55–66. doi:10.1016/j. chemgeo.2014.05.014

Huang, B., Tian, H., Li, X., Wang, Z., and Xiao, X. (2016). Geochemistry, Origin and Accumulation of Natural Gases in the Deepwater Area of the Qiongdongnan Basin, South China Sea. *Mar. Petroleum Geol.* 72, 254–267. doi:10.1016/j. marpetgeo.2016.02.007

Jiang, S., Yang, T., Ge, L., Yang, J., Ling, H., Wu, N., et al. (2008). Geochemistry of Pore Waters from the Xisha Trough, Northern South China Sea and Their Implications for Gas Hydrates. *J. Oceanogr.* 64, 459–470. doi:10.1007/s10872-008-0039-8

Jinhua, Z., Nianqiao, F., Wei, W., Ming, S., Hongping, X., Yong, P., et al. (2018). Accumulation Conditions and Enrichment Controlling Factors of Natural Gas Hydrate Reservoirs. *China Pet. Explor.* 23, 35.

Joye, S. B., Boetius, A., Orcutt, B. N., Montoya, J. P., Schulz, H. N., Erickson, M. J., et al. (2004). The Anaerobic Oxidation of Methane and Sulfate Reduction in Sediments from Gulf of Mexico Cold Seeps. *Chem. Geol.* 205, 219–238. doi:10.1016/ j.chemgeo.2003.12.019

Klinkhammer, G., Heggie, D. T., and Graham, D. W. (1982). Metal Diagenesis in Oxic Marine Sediments. *Earth Planet. Sci. Lett.* 61, 211–219. doi:10.1016/0012-821x(82)90054-1

Knittel, K., and Boetius, A. (2009). Anaerobic Oxidation of Methane: Progress with an Unknown Process. *Annu. Rev. Microbiol.* 63, 311–334. doi:10.1146/ annurev.micro.61.080706.093130

Kraemer, L. M., Owen, R. M., and Dickens, G. R. (2000). Lithology of the Upper Gas Hydrate Zone, Blake Outer Ridge: A Link between Diatoms, Porosity, and Gas Hydrate, Proceedings of the Ocean Drilling Program. *Sci. Results Tex. A&M Univ.* 144, 229–236.

Kvenvolden, K. A. (1995). A Review of the Geochemistry of Methane in Natural Gas Hydrate. *Org. Geochem.* 23, 997–1008. doi:10.1016/0146-6380(96) 00002-2

Kvenvolden, K. A. (1993). Gas Hydrates Geological Perspective and Global Change. *Rev. Geophys.* 31, 173–187. doi:10.1029/93rg00268

Lai, H., Fang, Y., Kuang, Z., Ren, J., Liang, J., Lu, J., et al. (2021). Geochemistry, Origin and Accumulation of Natural Gas Hydrates in the Qiongdongnan Basin, South China Sea: Implications from Site GMGS5-W08. *Mar. Petroleum Geol.* 123, 104774. doi:10.1016/j.marpetgeo.2020.104774

Larner, B. L., Seen, A. J., and Townsend, A. T. (2006). Comparative Study of Optimised BCR Sequential Extraction Scheme and Acid Leaching of Elements in the Certified Reference Material NIST 2711. *Anal. Chim. Acta* 556, 444–449. doi:10. 1016/j.aca.2005.09.058

Lemaitre, N., Bayon, G., Ondréas, H., Caprais, J., Freslon, N., Bollinger, C., et al. (2014). Trace Element Behaviour at Cold Seeps and the Potential Export of Dissolved Iron to the Ocean. *Earth Planet. Sci. Lett.* 404, 376–388. doi:10.1016/j. epsl.2014.08.014

Li, C., Hu, G., Zhang, W., Ye, Y., Liu, C., Li, Q., et al. (2016). Influence of Foraminifera on Formation and Occurrence Characteristics of Natural Gas Hydrates in Fine-Grained Sediments from Shenhu Area, South China Sea. *Sci. China Earth Sci.* 59, 2223–2230. doi:10.1007/s11430-016-5005-3

Li, L., Lei, X., Zhang, X., and Sha, Z. (2013). Gas Hydrate and Associated Free Gas in the Dongsha Area of Northern South China Sea. *Mar. Petroleum Geol.* 39, 92–101. doi:10.1016/j.marpetgeo.2012.09.007

Li, N., Feng, D., Chen, L., Wang, H., and Chen, D. (2016). Using Sediment Geochemistry to Infer Temporal Variation of Methane Flux at a Cold Seep in the South China Sea. *Mar. Petroleum Geol.* 77, 835–845. doi:10.1016/j.marpetgeo.2016. 07.026

Liang, J., Zhang, W., Lu, J. A., Wei, J., Kuang, Z., and He, Y. (2019). Geological Occurrence and Accumulation Mechanism of Natural Gas Hydrates in the Eastern Qiongdongnan Basin of the South China Sea: Insights from Site GMGS5-W9-2018. *Mar. Geol.* 418, 106042. doi:10.1016/j. margeo.2019.106042

Liang, Q., Hu, Y., Feng, D., Peckmann, J., Chen, L., Yang, S., et al. (2017). Authigenic Carbonates from Newly Discovered Active Cold Seeps on the Northwestern Slope of the South China Sea: Constraints on Fluid Sources, Formation Environments, and Seepage Dynamics. *Deep Sea Res. Part I Oceanogr. Res. Pap.* 124, 31–41. doi:10.1016/j.dsr.2017.04.015

Lin, Z., Sun, X., Chen, K., Strauss, H., Klemd, R., Smrzka, D., et al. (2022). Effects of sulfate reduction processes on the trace element geochemistry of sedimentary pyrite in modern seep environments. *Geochimica et Cosmochimica Acta.* 333, 75–94. doi:10.1016/j.gca.2022.06.026

Liu, S., Feng, X., Feng, Z., Xiao, X., and Feng, L. (2020). Geochemical Evidence of Methane Seepage in the Sediments of the Qiongdongnan Basin, South China Sea. *Chem. Geol.* 543, 119588. doi:10.1016/j.chemgeo.2020. 119588

Liu, W., Shi, Y., Zhang., X., Zeng, N., Y, J., and He, H., 2014. Geotechnical Features of the Seabed Soils in the East of Xisha Trough and the Mechanical Properties of Gas Hydrate-Bearing Fine Deposits. *Mar. Geol. Quat. Geol.* 34, 39–47.

Lu, H., Kawasaki, T., Ukita, T., Moudrakovski, I., Fujii, T., Noguchi, S., et al. (2011). Particle Size Effect on the Saturation of Methane Hydrate in Sediments-Constrained from Experimental Results. *Mar. Petroleum Geol.* 28, 1801–1805. doi:10.1016/j.marpetgeo.2010.11.007

Luff, R., and Wallmann, K. (2003). Fluid Flow, Methane Fluxes, Carbonate Precipitation and Biogeochemical Turnover in Gas Hydrate-Bearing Sediments at Hydrate Ridge, Cascadia Margin: Numerical Modeling and Mass Balances. *Geochimica Cosmochimica Acta* 67, 3403–3421. doi:10.1016/s0016-7037(03) 00127-3

Lyons, T. W., and Severmann, S. (2006). A Critical Look at Iron Paleoredox Proxies: New Insights from Modern Euxinic Marine Basins. *Geochimica Cosmochimica Acta* 70, 5698–5722. doi:10.1016/j.gca.2006.08.021

März, C., Hoffmann, J., Bleil, U., de Lange, G. J., and Kasten, S. (2008). Diagenetic Changes of Magnetic and Geochemical Signals by Anaerobic Methane Oxidation in Sediments of the Zambezi Deep-Sea Fan (SW Indian Ocean). *Mar. Geol.* 255, 118–130. doi:10.1016/j.margeo.2008.05.013

McLennan, S. M. (2001). Relationships between the Trace Element Composition of Sedimentary Rocks and Upper Continental Crust. *Geochem. Geophys. Geosyst.* doi:10.1029/2000gc000109

Moore, T. S., Murray, R. W., Kurtz, A. C., and Schrag, D. P. (2004). Anaerobic Methane Oxidation and the Formation of Dolomite. *Earth Planet. Sci. Lett.* 229, 141–154. doi:10.1016/j.epsl.2004.10.015

Morford, J. L., and Emerson, S. (1999). The Geochemistry of Redox Sensitive Trace Metals in Sediments. *Geochimica cosmochimica acta* 63, 1735–1750. doi:10. 1016/s0016-7037(99)00126-x

Murray, J. W., Grundmanis, V., and Smethie, W. M., Jr (1978). Interstitial Water Chemistry in the Sediments of Saanich Inlet. *Geochimica Cosmochimica Acta* 42, 1011–1026. doi:10.1016/0016-7037(78)90290-9

Nath, B., Jean, J., Lee, M., Yang, H., and Liu, C. (2008). Geochemistry of High Arsenic Groundwater in Chia-Nan Plain, Southwestern Taiwan: Possible Sources and Reactive Transport of Arsenic. *J. Contam. Hydrology* 99, 85–96. doi:10.1016/j. jconhyd.2008.04.005

Nevin, K. P., and Lovley, D. R. (2002). Mechanisms for Fe (III) oxide reduction in sedimentary environments. *Geomicrobiol. J.* 19, 141–159. doi:10.1128/AEM.68.5. 2294-2299.2002

Pape, T., Blumenberg, M., Seifert, R., Bohrmann, G., and Michaelis, W. (2008). Marine Methane Biogeochemistry of the Black Sea: a Review. *Links Between Geol. Process. Microb. Activities Evol. Life*, 281–311.

Peckmann, J., Reimer, A., Luth, U., Luth, C., Hansen, B. T., Heinicke, C., et al. (2001). Methane-derived Carbonates and Authigenic Pyrite from the Northwestern Black Sea. *Mar. Geol.* 177, 129–150. doi:10.1016/s0025-3227(01)00128-1

Peketi, A., Mazumdar, A., Joshi, R. K., Patil, D. J., Srinivas, P. L., and Dayal, A. M. (2012). Tracing the Paleo Sulfate-Methane Transition Zones and H_2S Seepage Events in Marine Sediments: An Application of C-S-Mo Systematics. *Geochem. Geophys. Geosystems* 13.

Poulton, S. W. S. P., and Canfield, D. E. D. B. (2005). Development of a Sequential Extraction Procedure for Iron: Implications for Iron Partitioning in Continentally Derived Particulates. *Chem. Geol.* 214, 209–221. doi:10.1016/j.chemgeo.2004.09.003

Raiswell, R., and Canfield, D. E. (2012). The Iron Biogeochemical Cycle Past and Present. *Geochem. Perspect.* 1, 1–220. doi:10.7185/geochempersp.1.1

Riedinger, N., Formolo, M. J., Lyons, T. W., Henkel, S., Beck, A., and Kasten, S. (2014). An Inorganic Geochemical Argument for Coupled Anaerobic Oxidation of Methane and Iron Reduction in Marine Sediments. *Geobiology* 12, 172–181. doi:10. 1111/gbi.12077

Ritger, S., Carson, B., and Suess, E. (1987). Methane-derived Authigenic Carbonates Formed by Subduction-Induced Pore-Water Expulsion along the Oregon/Washington Margin. *Geol. Soc. Am. Bull.* 98, 147–156. doi:10.1130/ 0016-7606(1987)98<147:macfbs>2.0.co;2

Scholz, F., McManus, J., Mix, A. C., Hensen, C., and Schneider, R. R. (2014a). The Impact of Ocean Deoxygenation on Iron Release from Continental Margin Sediments. *Nat. Geosci.* 7, 433–437. doi:10.1038/ngeo2162

Scholz, F., Severmann, S., McManus, J., and Hensen, C. (2014b). Beyond the Black Sea Paradigm: The Sedimentary Fingerprint of an Open-Marine Iron Shuttle. *Geochimica Cosmochimica Acta* 127, 368–380. doi:10.1016/j.gca.2013.11.041

Schulz, H. D., and Zabel, M. (2006). *Marine Geochemistry*. Netherland: Springer.

Scott, C., and Lyons, T. W. (2012). Contrasting Molybdenum Cycling and Isotopic Properties in Euxinic versus Non-euxinic Sediments and Sedimentary Rocks: Refining the Paleoproxies. *Chem. Geol.* 324, 19–27. doi:10.1016/j.chemgeo. 2012.05.012

Sha, Z., Liang, J., Zhang, G., Yang, S., Lu, J., Zhang, Z., et al. (2015). A Seepage Gas Hydrate System in Northern South China Sea: Seismic and Well Log Interpretations. *Mar. Geol.* 366, 69–78. doi:10.1016/j.margeo.2015.04.006

Shaohua, Q., Ming, S., Rui, Y., Zenggui, K., Jinqiang, L., and Nengyou, W. (2015). The Progress and Revelations of Marine Gas Hydrate Explorations: Reservoir Characteristics. *Adv. New Renew. Energy* 3, 357–366.

Smrzka, D., Feng, D., Himmler, T., Zwicker, J., Hu, Y., Monien, P., et al. (2020). Trace Elements in Methane-Seep Carbonates: Potentials, Limitations, and Perspectives. *Earth-Science Rev.* 208, 103263. doi:10.1016/j.earscirev.2020.103263

Su, L., Zheng, J., Chen, G., Zhang, G., Guo, J., and Xu, Y. (2012). The Upper Limit of Maturity of Natural Gas Generation and its Implication for the Yacheng Formation in the Qiongdongnan Basin, China. *J. Asian Earth Sci.* 54, 203–213. doi:10.1016/j.jseaes.2012.04.016

Sun, C., Wu, N., Niu, B., and Sun, Y. (2007). Geochemical Characteristics of Gaseous Hydrocarbons and Hydrate Resource Prediction in the Qiong-Dongnan Basin of the South China Sea. *Geoscience* 21, 95.

Tong, H., Feng, D., Cheng, H., Yang, S., Wang, H., Min, A. G., et al. (2013). Authigenic Carbonates from Seeps on the Northern Continental Slope of the South China Sea: New Insights into Fluid Sources and Geochronology. *Mar. petroleum Geol.* 43, 260–271. doi:10.1016/j.marpetgeo.2013.01.011

Torres, M. E., Brumsack, H. J., Bohrmann, G., and Emeis, K. C. (1996). Barite Fronts in Continental Margin Sediments: a New Look at Barium Remobilization in the Zone of Sulfate Reduction and Formation of Heavy Barites in Diagenetic Fronts. *Chem. Geol.* 127, 125–139. doi:10.1016/0009-2541(95)00090-9

Tribovillard, N., Algeo, T. J., Baudin, F., and Riboulleau, A. (2012). Analysis of Marine Environmental Conditions Based on Molybdenum-Uranium Covariation-Applications to Mesozoic Paleoceanography. *Chem. Geol.* 324-325, 46–58. doi:10.1016/j.chemgeo.2011.09.009

Tribovillard, N., Algeo, T. J., Lyons, T., and Riboulleau, A. (2006). Trace Metals as Paleoredox and Paleoproductivity Proxies: An Update. *Chem. Geol.* 232, 12–32. doi:10.1016/j.chemgeo.2006.02.012

Tribovillard, N., Du Châtelet, E. A., Gay, A., Barbecot, F., Sansjofre, P., and Potdevin, J. (2013). Geochemistry of Cold Seepage-Impacted Sediments: Per-Ascensum or Per-Descensum Trace Metal Enrichment? *Chem. Geol.* 340, 1–12. doi:10.1016/j.chemgeo.2012.12.012

Uchida, T., and Tsuji, T. (2004). Petrophysical Properties of Natural Gas Hydrates-Bearing Sands and Their Sedimentology in the Nankai Trough. *Resour. Geol.* 54, 79–87. doi:10.1111/j.1751-3928.2004.tb00189.x

Udden, J. A. (1914). Mechanical Composition of Clastic Sediments. *Geol. Soc. Am. Bull.* 25, 655–744. doi:10.1130/gsab-25-655

Vargas-Cordero, I., Tinivella, U., Villar-Muñoz, L., Bento, J. P., Cárcamo, C., López-Acevedo, D., et al. (2020). Gas Hydrate versus Seabed Morphology Offshore Lebu (Chilean Margin). *Sci. Rep.*, 21928. doi:10.1038/s41598-020-78958-z10

Wang, S., Wen, Y., and Song, H. (2006). Mapping the Thickness of the Gas Hydrate Stability Zone in the South China Sea. TAO: Terrestrial. *Atmos. Ocean. Sci.* 17, 815.

Wang, X. J., Wu, S. G., Wang, D. W., Ma, Y., Yao, G., and Gong, Y. (2010). The Role of Polygonal Faults in Fluid Migration and Gas Hydrate Reservoir Forming in Southeast Hainan Basin. Oil Geophys. *Prospect* 45, 122–128.

Wang, X., Li, N., Feng, D., Hu, Y., Bayon, G., and Liang, Q. (2018). Using chemical compositions of sediments to constrain methane seepage dynamics: A case study from Haima cold seeps of the South China Sea. *J. Asian Earth Sci.* 168, 137–144. doi:10.1016/j.jseaes.2018.11.011

Waseda, A. (1998). Organic Carbon Content, Bacterial Methanogenesis, and Accumulation Processes of Gas Hydrates in Marine Sediments. *Geochem. J.* 32, 143–157. doi:10.2343/geochemj.32.143

Wei, D., Jinqiang, L., Wei, Z., Zenggui, K., Tong, Z., and Yulin, H. (2021). Typical Characteristics of Fracture-Filling Hydrate-Charged Reservoirs Caused by Heterogeneous Fluid Flow in the Qiongdongnan Basin, Northern South China Sea. *Mar. Petroleum Geol.* 124, 104810. doi:10.1016/j.marpetgeo.2020.104810

Wei, J., Fang, Y., Lu, H., Lu, H., Lu, J., Liang, J., et al. (2018). Distribution and Characteristics of Natural Gas Hydrates in the Shenhu Sea Area, South China Sea. *Mar. Petroleum Geol.* 98, 622–628. doi:10.1016/j.marpetgeo.2018.07.028

Wei, J., Liang, J., Lu, J., Zhang, W., and He, Y. (2019). Characteristics and Dynamics of Gas Hydrate Systems in the Northwestern South China Sea - Results of the Fifth Gas Hydrate Drilling Expedition. *Mar. Petroleum Geol.* 110, 287–298. doi:10.1016/j.marpetgeo.2019.07.028

Wu, N., Yang, S., Zhang, H., Liang, J., Wang, H., Su, X., et al. (2008). "Preliminary Discussion on Gas Hydrate Reservoir System of Shenhu Area, North Slope of South China Sea," in Proceedings of the 6th International Conference on Gas Hydrates (ICGH 2008), Vancouver. British Columbia, Canada, July 6-10, 2008.

Wu, S., Zhang, G., Huang, Y., Liang, J., and Wong, H. K. (2005). Gas Hydrate Occurrence on the Continental Slope of the Northern South China Sea. *Mar. Petroleum Geol.* 22, 403–412. doi:10.1016/j.marpetgeo.2004.11.006

Xu, X. D., Zhang, Y. Z., Liang, G., Xiong, X., Xing, L., Guo, X., et al. (2016). Hydrocarbon Source Condition and Accumulation Mechanism of Natural Gas in Deepwater Area of Qiongdongnan Basin, Northern South China Sea. *Nat. Gas. Geosci.* 27, 1985–1992.

Yang, H., Lu, H., and Ruffine, L. (2018). Geochemical Characteristics of Iron in Sediments from the Sea of Marmara. *Deep Sea Res. Part II Top. Stud. Oceanogr.* 153, 121–130. doi:10.1016/j.dsr2.2018.01.010

Yang, K., Chu, F., and Zhu, J. (2014). Mg/Ca and Sr/Ca Ratios of Authigenic Carbonate Minerals and Calcareous Biogenic Shells in the Cold-Seep Acrbonates, North of the South China Sea and Their Environmental Implication. *Haiyang Xuebao (in Chin.* 36, 39–48.

Ye, J., Wei, J., Liang, J., Lu, J., Lu, H., and Zhang, W. (2019). Complex Gas Hydrate System in a Gas Chimney, South China Sea. *Mar. Petroleum Geol.* 104, 29–39. doi:10.1016/j.marpetgeo.2019.03.023

Ye, Z. Z., He, Q. X., and Zhang, M. S. (1985). Sedimentary Structure and Facies Pattern of Bioarenaceous Limestone in Late Pleistocene of Xisha Shidao. Acta Sedimentol. *Sin* 3, 1–15.

Zhang, G., Huang, Y., Zhu, Y., and Wu, B. (2002). Prospect of Gas Hydrate Resources in the South China Sea. *Mar. Geol. Quat. Geol.* 22, 75–82.

Zhang, G., Liang, J., Yang, S., Zhang, M., Holland, M., Schultheiss, P., et al. (2015). Geological Features, Controlling Factors and Potential Prospects of the Gas Hydrate Occurrence in the East Part of the Pearl River Mouth Basin, South China Sea. *Mar. Petroleum Geol.* 67, 356–367. doi:10.1016/j.marpetgeo.2015.05.021

Zhang, H. Q., Yang, S. X., Wu, N. Y., Su, X., Holland, M., Schultheiss, P., et al. (2007). Successful and Surprising Results for China's First Gas Hydrate Drilling Expedition. *Fire Ice* 7, 6–9.

Zhang, M. Z. M., Lu, H. L. H., Guan, H. G. H., Liu, L. L. L., Wu, D. W. D., and Wu, N. W. N. (2018). Methane Seepage Intensities Traced by Sulfur Isotopes of Pyrite and Gypsum in Sediment from the Shenhu Area, South China Sea. *Acta Oceanol. Sin.* 37, 20–27. doi:10.1007/s13131-018-1241-1

Zhang, W., Liang, J., Lu, J., Wei, J., Su, P., Fang, Y., et al. (2017). Accumulation Features and Mechanisms of High Saturation Natural Gas Hydrate in Shenhu Area, Northern South China Sea. *Petroleum Explor. Dev.* 44, 708–719. doi:10.1016/s1876-3804(17)30082-4

Zhang, W., Liang, J., Su, P., Wei, J., Gong, Y., Lin, L., et al. (2019). Distribution and Characteristics of Mud Diapirs, Gas Chimneys, and Bottom Simulating Reflectors Associated with Hydrocarbon Migration and Gas Hydrate Accumulation in the Qiongdongnan Basin, Northern Slope of the South China Sea. *Geol. J.* 54, 3556–3573. doi:10.1002/gj.3351

Zhao, Q., Jian, Z., Li, B., Cheng, X., and Wang, P. (1999). Microtektites in the Middle Pleistocene Deep-Sea Sediments of the South China Sea*. *Sci. China Ser. D-Earth. Sci.* 42, 531–535. doi:10.1007/bf02875247

Zhou, Y. A., Di, P. B. C. D., Li, N. B. C. D., Chen, F. A., Su, X. F., and Zhang, J. A. (2020). Unique Authigenic Mineral Assemblages and Planktonic Foraminifera Reveal Dynamic Cold Seepage in the Southern South China Sea. *Minerals* 10, 275–287. doi:10.3390/min10030275

Zhu, W., Huang, B., Mi, L., Wilkins, R. W., Fu, N., and Xiao, X. (2009). Geochemistry, Origin, and Deep-Water Exploration Potential of Natural Gases in the Pearl River Mouth and Qiongdongnan Basins, South China Sea. *Am. Assoc. Pet. Geol. Bull.* 93, 741–761. doi:10.1306/02170908099